

# EC-Heating for W7-X: physics and technology

V. Erckmann<sup>1</sup>, P. Brand<sup>3</sup>, H. Braune<sup>1</sup>, G. Dammertz<sup>2</sup>, G. Gantenbein<sup>2</sup>,  
W. Kasparek<sup>3</sup>, H. P. Laqua<sup>1</sup>, H. Maassberg<sup>1</sup>, N. B. Marushchenko<sup>1</sup>, G. Michel<sup>1</sup>,  
M. Thumm<sup>2</sup>, Y. Turkin<sup>1</sup>, M. Weissgerber<sup>1</sup>, A. Weller<sup>1</sup>, and the W7-X ECRH- teams at IPP  
Greifswald<sup>1</sup>, FZK Karlsruhe<sup>2</sup> and IPF Stuttgart<sup>3</sup>

*1 Max Planck Institut für Plasmaphysik, EURATOM Association,*

*Teilinstitut Greifswald, D-17491 Greifswald, Germany*

*2 Forschungszentrum Karlsruhe, Association EURATOM-FZK, IHM,*

*Hermann-von-Helmholtz-Platz 1, D-76344 Eggenstein-Leopoldshafen, Germany,*

*3 Institut für Plasmaforschung, Universität Stuttgart, D-70569 Stuttgart, Germany*

Information on the corresponding author:

Volker Erckmann

*Max Planck Institut für Plasmaphysik,*

*Wendelsteinstrasse 1, D-17491 Greifswald, Germany*

e-mail: [volker.erckmann@ipp.mpg.de](mailto:volker.erckmann@ipp.mpg.de)

Phone: +49-3834-88-2450 Fax: +49-3834-88-2459

Pages: 73 (incl. ref., tables, Figures and Fig. captions)

Tables: 3

Figures: 27 (should be published in colors)

**Abstract:**

The W 7-X Stellarator ( $R = 5.5$  m,  $a = 0.55$  m,  $B < 3.0$  T), which is presently being built at IPP-Greifswald, aims at demonstrating the inherent steady state capability of stellarators at reactor relevant plasma parameters. A 10 MW ECRH plant with cw-capability is under construction to meet the scientific objectives. The physics background of the different heating- and current drive scenarios is presented. The expected plasma parameters are calculated for different transport assumptions. A newly developed ray tracing code is used to calculate selected reference scenarios and optimize the EC-launcher and in-vessel structure. Examples are discussed and the technological solutions for optimum wave coupling are presented. The ECRH plant consists of 10 RF-modules with 1 MW power each at 140 GHz. The RF-beams are transmitted to the W7-X torus (typically 60 m) via two open multi-beam mirror lines with a power handling capability, which would already satisfy the ITER requirements (24 MW). Integrated full power, cw tests of two RF-modules (gyrotrons and the related transmission line sections) are reported and the key features of the gyrotron- and transmission line technology are presented. As the physics and technology of ECRH for both W7-X and ITER has many similarities, test results from the W7-X ECRH may provide valuable input for the ITER-ECRH plant.

PACS: 52.50.-b, 52.25.Xz, 52.55.-s, 52.50.Gj, 41.20.Jb, 84.40.-x.

## I. INTRODUCTION

The physics goals for the W7-X Stellarator determine the main machine parameters as well as a consistent set of heating systems, diagnostics, data acquisition and machine control. W7-X ( $R = 5.5$  m,  $a = 0.55$  m) is the next step in the Stellarator approach towards magnetic fusion power plants. In contrast to Tokamaks, Stellarators have inherent steady state operation capability, because the confining magnetic field is generated by external coils only. The scientific objectives for W7-X can be formulated as follows:

1. Demonstration of quasi steady state operation at reactor relevant parameters
2. Demonstration of good plasma confinement
3. Demonstration of stable plasma equilibrium at a reactor relevant plasma pressure  $\beta$  of about 5 %
4. Investigation and development of a divertor to control plasma density, energy and impurities.

W7-X is equipped with a superconducting coil system, a continuously operating heating system and an actively pumped divertor for stationary particle and energy control. The outline design is seen from Fig.1. In contrast to ITER, W7-X does not aim at DT-operation and provisions for remote handling in a radioactive environment are not foreseen. ECRH is the main heating system for steady state operation. The high- $\beta$  criterion will be addressed in pulsed experiments ( $< 10$  s) at reduced magnetic field in a later state of the machine operation, where Neutral Beam Injection Heating will be available with 20 MW for 10 s.

An ECR-heating power of 10 MW is required to achieve the envisaged plasma parameters [1] at the nominal magnetic field of 2.5 T. The standard heating and current drive scenario is 2<sup>nd</sup> harmonic extraordinary mode (X2) with low field side launch. High-density

operation above the X2 cut-off density at  $1.2 \cdot 10^{20} \text{ m}^{-3}$  is accessible with 2<sup>nd</sup> harmonic ordinary mode (O2,  $n_e < 2.5 \cdot 10^{20} \text{ m}^{-3}$ ) and at even higher densities with O-X-Bernstein-wave (OXB) mode conversion heating [2,3]. Theoretical investigations show, that 3<sup>rd</sup> harmonic extraordinary mode (X3) heating ( $B_{\text{res}} = 1.66 \text{ T}$ ,  $n_e < 1.6 \cdot 10^{20} \text{ m}^{-3}$ ) is a promising scenario for operation at reduced magnetic field, and would extend the operation-flexibility further. As W7-X has no OH-transformer for inductive current drive, EC-current drive is a valuable tool to modify the internal current density distribution and to counteract residual bootstrap currents. A new ray-tracing code was developed and used to investigate the different ECRH-operation scenarios in combination with transport modeling. A brief description of the codes and some selected results on ECRH-operation scenarios are discussed in Sec. II. The predicted plasma parameters are calculated with a new transport code for a conservative and a more optimistic approach. The total ECRH power is generated by 10 gyrotrons operating at 140 GHz with 1 MW output power in cw operation each. The construction of the ECRH-plant is in a well-advanced state, the general design features and the status of both the gyrotron and transmission line commissioning is presented in Sec. III together with recent results from integrated full performance tests. The ECRH-launcher and the related in-vessel structures must satisfy different demands for all proposed operation scenarios. The resulting technological solutions are presented in Sec. IV.

The physics demands for both, W7-X and ITER request a versatile and flexible ‘day one’ ECRH-system with high reliability. Some basic features of both systems are compared in Table I, the similarities are obvious with the ITER installation having about twice the power:

## **II. W7-X OPERATION SCENARIOS WITH ECRH**

The heating scenarios discussed below will cover a wide density range for W7-X experiments. We distinguish roughly between two density branches, below and above  $1 \cdot 10^{20}$

$\text{m}^{-3}$ . Below this value, X2-mode heating is the standard method and the experiments may concentrate in this range on transport and magnetic configuration investigations. Above this density, more sophisticated operation scenarios like O2-mode, X3-mode and O-X-B mode conversion heating have to be applied. Fig. 2 sketches the accessible density for different heating scenarios. High-density operation is favorable for efficient divertor operation and thus experiments in this regime may focus on the divertor-physics and particle/impurity control.

## II.A Numerical tools for predictive investigations

A new ray tracing code was developed for electron cyclotron wave studies in arbitrary 3D magnetic configurations, with emphasis on heating, current drive and ECE diagnostics. The ray tracing equations are the standard Hamiltonian ones. Generally, the ‘cold’, ‘warm’ non-relativistic, or weakly relativistic dielectric tensor can be used in the Hamiltonian. With the weakly relativistic dielectric tensor, the model of tracing includes those kinetic effects which become significant in the vicinity of the EC resonance, leading to ‘anomalous’ dispersion effects and possible wiggling and even bending of the rays there [4,5]. For example, in contrast with the ‘cold’ approach (which should be sufficient for many cases), the weakly relativistic model can give a quite different result in the case of (quasi-vertical) launch with the ray trajectories almost tangential to the resonance line, i.e. in the vicinity of the resonance, but along a direction with small magnetic field gradient.

Quantities such as the absorption and emissivity are calculated in fully relativistic approach separately for passing and trapped electrons with an arbitrary electron distribution function. For calculations of ECCD efficiency, the adjoint approach (with momentum

conservation) is used in either collisional or collisionless limits [2,6]. The code also incorporates the module from the ART code [7] to treat the OXB-mode conversion.

The magnetic configuration is provided by the 3D equilibrium code VMEC [8]. A highly optimized geometrical module is used for fast transformations between Cartesian and magnetic coordinates. The code is used through an especially designed graphical user interface, which allows the preparation of input parameters and viewing simulation results in convenient (2D and 3D) form. With this interface the code is easily operated from any interested user.

The code was partly benchmarked against the ‘old’ W7-AS [2], the TORBEAM [9], and the WR\_RTC [10] codes. Additionally, successful tests were performed on the ITER reference ‘*Scenario 2*’ against several other code predictions. The code-package is now routinely exploited in modeling heating at various harmonics of the O and X-mode (O1, O2, X2 and X3) in different magnetic configurations and is extensively used to support the design of ECRH launcher components for W7-X (see Sec. IV).

For the ray-tracing calculations, it is necessary to specify the plasma temperature and density. The relationship between density and temperature profiles is determined by the heating power and the confinement properties of the device. The results of transport modeling for the W7-X stellarator are presented in the next section. To model transport in W7-X, we use a predictive 1-D transport code which is under development [11]. So far a set of reference calculations assuming neoclassical confinement plus anomalous contributions (dominant at low density and temperature) has been carried out for the case of X2-mode heating.

## II.B X2 Heating from LFS in the equatorial plane

X2-heating is the standard method for plasma start-up and “low” density ( $< 1.2 \cdot 10^{20} \text{ m}^{-3}$ ) operation. The single pass absorption is sufficiently high that nearly total absorption is guaranteed even close to the cut-off density ( $< 1.2 \cdot 10^{20} \text{ m}^{-3}$ ). The modeling of transport in W7-X predicts that the heating power of 10 MW is sufficient to obtain an electron temperature in the range of 10 - 25 keV at low density and about 4 - 8 keV at  $1.0 \cdot 10^{20} \text{ m}^{-3}$ , see Fig.3 (top). The numbers depend, of course, on the assumption for the electron heat diffusivity and on the assumed radial location of the power deposition. An example is given in Fig. 3 (bottom), where the radial structure of the electron heat diffusivity is compared for a conservative assumption based on the ISS95 confinement scaling [12] and a much more optimistic approach assuming neoclassical heat diffusivity in the bulk plasma (which are the minimum possible losses) plus anomalous transport near the plasma edge. The central density in Fig.3 (bottom) is  $n_{e0} = 0.6 \cdot 10^{20} \text{ m}^{-3}$  for both cases. The resulting central electron temperature is around 5 keV for the conservative assumption, the  $n_e$  and  $T_e$  profiles for the neoclassical (plus anomalous contribution) approach are shown in Fig. 4. The latter modeling is performed using a new 1-D transport code [11]. It should be noted, that W7-X is, among other criteria, optimized with respect to neoclassical transport, the predictions therefore lead to surprisingly high electron temperatures. We wish to point out, however, that neoclassical behavior in the bulk plasma was found at W7-AS under optimized conditions [13] and electron temperatures up to 6.8 keV were measured already in this comparatively small device.

For the evaluation of neoclassical transport we use a dataset of transport coefficients calculated by the DKES-code [14]. In the simulation we determine self-consistently the neoclassical fluxes and the radial electric field, which strongly affects the transport at low collisionality. In the region of a high gradient of the density the electron and ion anomalous

heat conductivities are taken in the form  $\propto 1/n_e$  with exponential decay towards the center of the plasma. This choice is supported by W7-AS results [15], where the anomalous heat diffusivity obtained from power balance analysis decreases with increasing  $n_e$  at the edge. During the calculations, the shape of the density profile is kept fixed. For simplicity we use a prescribed ECRH power deposition profile

$$P_{ECRH} \propto \exp\left(- (r - r_c)^2 / w^2\right),$$

where  $r_c$ ,  $w$  are the location and width of the heating source.

In Fig. 4 the density and temperatures along with the calculated radial electric field are shown for the case of central density  $0.6 \cdot 10^{20} \text{ m}^{-3}$  and 4 MW of slightly off-axis ECRH. In the plasma center, the ‘electron root’ with the positive electric field is seen. For higher density and the same heating conditions the ‘electron root’ disappears and the electric field becomes negative throughout the entire plasma.

### **II.C O2 and X3 Heating from LFS in the equatorial plane**

At intermediate densities ( $< 2.4 \cdot 10^{20} \text{ m}^{-3}$ ) a heating scenario with multi-pass absorption of the O2-mode was developed. As this mode has a single pass absorption of 50-80% depending on the plasma parameters, which are calculated assuming ISS95-confinement scaling, as shown in Fig.5 (left), the transmitted power fraction would thermally overload the standard graphite wall protection tiles opposite to the ECRH launchers. Therefore 12 selected tiles will be replaced by highly reflecting metallic tiles (TZM, molybdenum alloy), for details see Sec. IV.B. The reflector position and orientation was optimized by ray-tracing calculations such, that the reflected beam passes through the plasma center, too. This increases the heating efficiency significantly and reduces the level of the non-absorbed ECRH stray-radiation.

The same reflecting tiles can also be used for X3-mode heating at a reduced resonant magnetic field of 1.66 T. The optimum oblique launch angle for both heating scenarios is about  $12^\circ$  at the most elongated plasma cross-section position. An example for the ray-tracing calculation is shown in Fig. 6 for a density close to the cut-off density ( $n_e(0) = 1.5 \cdot 10^{20} \text{ m}^{-3}$ ). The beam deflection by plasma refraction is below 30 mm at the tiles, which can be easily compensated by the movable antennas. The beam position as well as the transmitted power will be measured by microwave pick-up horns, which are integrated in the reflecting tiles.

## II.D O2-Heating from the High-Field Side

Two ports are available at W7-X for physics investigations with High Field Side (HFS) launch of ECRH with a maximum power of 2 MW. Here we make use of a peculiarity of the W7-X magnetic field configuration, which has a strong variation of the plasma cross-section as well as a strongly varying magnetic field. The ‘bean shaped’ poloidal cross-section (see Fig. 6) at  $\phi = 0^\circ$  has a tokamak-like magnetic field gradient and is used therefore for LFS-launch in the equatorial plane. The poloidal plasma cross-section changes from ‘bean shaped’ to a ‘triangular’ shape moving from  $\phi = 0^\circ$  to  $\phi = 36^\circ$  in toroidal direction. This cross-section is characterized by a minimum of  $B$  (for the standard configuration used in the simulations,  $B_{\text{max}}/B_{\text{min}} \cong 1.09$  on axis). The magnetic field shows a very weak, inverse gradient in this plane for some poloidal angular range, where we have placed additional ports for ECRH.

The simulation is performed for  $B_0 = 2.7 \text{ T}$  (as the reference the axial value of  $B$  on the “bean-shaped” cross-section is chosen, i.e.  $B_0 \equiv B_0(\phi = 0)$ ),  $n_e = 1.5 \cdot 10^{20} \text{ m}^{-3}$ , and  $T_e = 3 \text{ keV}$

with almost flat core profiles. The Gaussian beam with an initial width of 10 cm is discretized by 80 rays. Because of high density, refraction of the launched beam is significant and does not allow the focusing of the beam on axis (Fig.7, (a)). Since the plasma is “optically gray” for O2-mode, the deposition profile,  $p(r_{\text{eff}}) \equiv dP_{\text{abs}}/dV$  (absorbed power per unit volume), is quite broad (Fig.7 (b)), and the power shine-trough is about 13% (Fig.7, (c)). The most important result (and even somewhat surprising for the O-mode) is that about 60% of power is absorbed by ripple-trapped electrons (Fig.7 (c)). Furthermore, the shapes of the deposition profiles for trapped and passing electrons ( $p_t(r_{\text{eff}})$  and  $p_p(r_{\text{eff}})$ , respectively, with  $p = p_t + p_p$ ) are quite different (Fig.7 (b)). The damping along the ray becomes significant starting from  $r_{\text{eff}}/a \leq 0.7$  with the cyclotron interaction velocity range (not shown)  $v/v_{th} \approx 3$ , where the absorption by trapped electrons is dominant. In the region  $r_{\text{eff}}/a < 0.4$ , where the interaction velocity range is decreased up to  $v/v_{th} \approx 1.5$ , mainly passing electrons are responsible for damping. The optical depth is still not so high there,  $\tau \approx 1-1.5$  (plasma is gray), and the rays contain quite enough power to heat also the passing electrons. For comparison, simulation for X2-scenario (almost the same launch conditions, but reduced density,  $n_e = 0.5 \cdot 10^{20} \text{ m}^{-3}$ , and magnetic field increased up to  $B_0 = 2.68 \text{ T}$ ), gives quite similar  $p_t(r_{\text{eff}})$  and  $p_p(r_{\text{eff}})$ , and the damping by passing electrons is dominating. For the X2-mode, the plasma is optically thick with well localized damping, and the conditions within the absorption region are almost unchanged.

Note, that this O2 feature is specific for the W7-X configurations and for the HFS launch scenario. Nevertheless, it demonstrates a flexibility of the W7-X, where the fraction of trapped particles in the “triangular” plane can be varied in configuration scans. This adds to the flexibility of the launcher.

## II.E O-X-B Mode Conversion Heating (equatorial launch)

High-density operation above the O2-mode cut-off ( $2.5 \cdot 10^{20} \text{ m}^{-3}$ ) may become an attractive operation regime, because favorable plasma confinement, the so called High Density H-Mode (HDH) was discovered at W7-AS with plasma densities up to  $4 \cdot 10^{20} \text{ m}^{-3}$  [16,17]. This regime is only accessible with Electron Bernstein Wave (EBW) Heating, which can be excited by the OXB-conversion process. EBWs do not suffer from any upper density limit and have a high absorption near the cyclotron harmonics. OXB-conversion heating was successfully applied at the W7-AS stellarator [3, 18]. The EBWs are excited by an oblique launch of O-mode, which converts into a slow X-mode at the O-mode cutoff, and, finally, into EBWs in the vicinity of the upper-hybrid resonance. The required launch angle for the O2-mode is typically  $35^\circ$ , which is supported by the actual antenna design. First ray-tracing calculations on EBW-power deposition have been started recently. The experimental situation was simulated by launching the microwave beam from the ECRH- ports at the LFS near the ‘bean shaped’ plane with an optimal angle (i.e. with O-X conversion efficiency more than 99%). In this cross-section the magnetic field reaches its maximum, hence the number of trapped particles is close to zero. The frequency and the magnetic field on axis are  $f = 140$  GHz and  $B_0 = 2.2$  T, respectively, corresponding to  $\omega \approx n\omega_{ce}$  as the lowest (and dominating) resonance for damping. Reasonable plasma core parameters were chosen as  $n_e = 3 \cdot 10^{20} \text{ m}^{-3}$  and  $T_e(0) = 1$  keV. The resulting ray trajectory is shown in Fig.8, along with the evolutions of the refractive index components  $N_\perp$ ,  $N_\parallel$  and the pitch between the wave vector and the group velocity. Just to illustrate the features of EBW propagation, the ray trajectory shown is significantly prolonged after its complete absorption. The expected behavior of the refractive index is observed: after the conversion into EBW  $N_\perp$  grows up to large values,

$N_{\perp} \gg 1$ , while  $N_{\parallel} \approx 1$  (Fig.8, (b)). Note also that the pitch between the wave vector and the group velocity  $v_{gr}$  inverts its sign (Fig. 8, (c)), which is the sign of the “backward propagation” of EBWs. The power is absorbed near the axis, producing well localized deposition profile (not shown here).

## II.F EC-Current Drive

The W7-X magnetic configuration minimizes plasma net currents, such as the pressure driven bootstrap current. Residual bootstrap currents are expected to be small and are in the range up to 20 kA. As W7-X has no OH-transformer for inductive current compensation, ECCD is a good candidate to counteract residual plasma net currents and thus control the rotational transform  $\iota$ . ECCD may also be used to control of the divertor strike point position by controlling the edge rotational transform on an intermediate time-scale. For long time scales,  $\iota$  will be controlled by the external coil currents. For fine-tuning of the magnetic islands at the divertor, additional correction coils are available. In Fig.9 we have plotted the current drive efficiency as a function of the launch angle for different densities in the standard heating scenario X2. The related electron temperatures are roughly consistent with the ISS95 scaling and thus provide a conservative estimate for the CD-efficiency. Calculations with the new ray tracing code confirmed the ECCD results obtained earlier [2]. Up to 300 kA current are predicted at  $1.0 \cdot 10^{19} \text{ m}^{-3}$  by ECCD. Even at  $1.0 \cdot 10^{20} \text{ m}^{-3}$  an ECCD current around 25 kA was estimated, which is sufficient to compensate the expected bootstrap current. As seen from Fig.9, the launch angle scan shows a flat maximum for all densities around  $13^{\circ}$ . The numerical scan was performed keeping the magnetic field fixed, which corresponds to the experimental conditions. Note, that the resonance layer shifts

radially outward with increasing launch angle due to Doppler shift and beam diffraction. For simplicity, the scan was performed using one central ray only. The ECRH-launcher is designed to cope with the optimum launch angle for all 10 beams in co- and counter direction, for details see Sec. IVA. Beside the standard low field side oblique launch, two special ports (N-type) for advanced current drive scenarios are foreseen. Through this port the beam can be launched along the resonant surface with  $B=\text{const}$ , which allows to localize and investigate the wave-particle interaction in the velocity space.

## II.G Plasma- $\beta$ with ECRH

Following the philosophy of the previous section II.B, where we have compared predicted plasma parameters for conservative (ISS95) [12] and optimistic [11] transport assumptions, we compare the predicted plasma  $\beta$  for both cases. Please note, that the stability  $\beta$ -limit for W7-X is expected around 5 %. The exploration of this limit is one of the most important scientific objectives of W7-X. The high-density regime was investigated at W7-AS [19] and a density limit was derived [20], which depends on the absorbed power density and magnetic field as  $n_{dl} = 1.46(P/V)^{0.48} B^{0.54}$ . The corresponding beta limit  $\beta \propto \tau_E P / V B^2$  is the result of the density limit expression and the formula for energy confinement time  $\tau_E$ . Fig. 10 shows the power dependence of the highest possible beta derived from the different  $\tau_E$ -scaling laws for the cases of the X2, O2, and X3 heating scenarios. The two bottom curves are the predictions based on the W7-AS energy confinement time, which is the improved ISS95-scaling  $\tau_E = 1.5 \tau_E^{ISS95} = 1.5 \cdot 0.256 a^{2.21} R^{0.65} P^{-0.59} n^{0.51} B^{0.83} t_{2/3}^{0.4}$ . The solid curve represents the beta limit for the second harmonic heating at the magnetic field  $B \approx 2.5\text{T}$ . The backslash sign on the curve denotes the heating power at which the cut-off

density limit is reached in the X2 scenarios. The dashed curve stands for the X3 heating at  $B \approx 1.66\text{T}$  and shows no cut-off density limit within the available heating power.

The two upper curves marked by circles are the ‘more optimistic’ predictions for the beta limit based on the energy confinement time  $\tau_E^{predictive} = 1.32 a^{2.21} R^{0.65} P^{-0.59} n^{0.8} B^{0.83} t_{2/3}^{0.4}$  derived from the recent transport modeling, see section II B. The dashed curve shows the dependence of the beta limit on the absorbed power for the case of X3 heating. For the X2 heating scenario the cut-off density limit is reached at 7.5 MW power, where  $\beta \approx 4.5\%$ , see the solid curve marked by circles till backslash mark. A further increase of the heating power would increase the temperatures at constant density (near the cut-off) density. For the O2 heating scenario no such restrictions exist within the available ECRH power range. Although significant  $\beta$ -values are predicted even in the conservative transport approach, it is evident, that in this case the physics of the W7-X  $\beta$ -limit cannot be explored with ECRH alone. A 20 MW NBI-system in pulsed operation ( $< 10$  s) is therefore foreseen at W7-X to address the  $\beta$ -limit physics at reduced magnetic field. ECRH may assist with plasma start-up at 70 GHz (X2,  $B_{res} = 1.25$  T), which is an option and is not realized up to now.

### III. THE ECRH-PLANT

The design of the ECRH system took full advantage of the fact, that the ECRH-building could be tailored exactly to the needs of ECRH as seen in Fig. 11. The 10 gyrotrons operating at 140 GHz (plus two optional tubes at 70 GHz for plasma start up at low magnetic field) and the auxiliary systems (high-voltage supplies, water cooling, liquid helium and liquid nitrogen supplies for the gyrotron magnets are placed in a separate ECRH building adjacent to the central W7-X experimental hall.

The gyrotrons are installed in two rows symmetrically to a central underground beam duct, which connects the ECRH hall with the stellarator. To achieve maximum reliability and availability, we have chosen a modular design, which allows commissioning and operation of each gyrotron and the required subsystems independently from all others. Repair or maintenance of one module is possible without affecting the operation of all other gyrotrons. This design also minimizes the costs because series production of identical modules is possible. It is evident from this concept, that the demonstration of cw-operation at full power with a single module, which was achieved recently, gives high confidence in the full system capability. An optical transmission system was developed for W7-X, which is the most simple, reliable and cost effective solution. The transmission of the RF-power to the torus (typically 60 m) is performed by two open multi-beam mirror lines, each of them combining and handling 5 (+2) individual RF-beams (7 MW). The power handling capability has inherently a large safety margin (factor of 2-3) due to the low power density on the mirror surfaces. This keeps the option open to replace the 1 MW gyrotrons by more powerful ones in a later state, if such gyrotrons become available. It is worth noting, that the W7-X transmission system satisfies the ITER-ECRH (24 MW) power capability demands without modification at a somewhat lower safety margin. An underground concrete duct houses the individual components of the transmission system, the concrete walls are an efficient absorber of stray radiation from the open lines thus satisfying the safety-requirements on microwave shielding. All mirrors in the beam duct are remotely controlled.

### III.A The W7-X gyrotron

The development of cw-gyrotrons with an output power in the megawatt range for fusion application was and still is subject of a worldwide R&D effort, which is mainly driven by the needs of the two large fusion devices W7-X and ITER.

The development of the ‘W7-X gyrotron’ started in 1998 in Europe with Thales Electron Devices (TED) and in USA with CPI as industrial partners. Some important design parameters for both development lines are summarized in Table II. The design approach for both gyrotrons includes single-stage collector depression to enhance the efficiency and relax the collector loading. Both are ‘diode-type’ gyrotrons with no control anode to simplify the design. The collector is at ground potential, the depression voltage (cavity and body) has positive, the cathode voltage has negative polarity, respectively. The output vacuum window [21] uses a single edge-cooled disk of chemical vapor-deposited diamond (CVD-diamond) with an outer diameter of 106 mm, a thickness of 1.8 mm (four half wavelengths) and a window aperture of 88 mm. The RF-cavities operate in the  $TE_{28,8}$  mode (TED) and  $TE_{28,7}$  (CPI), respectively.

Results from the two R&D tubes from TED are reported in [22], results from the R&D at CPI are reported in [23,24,25], respectively.

The cavity design for the TED gyrotron features a linear input taper and a non-linear output taper. Special care has been taken for the design of the quasi-optical mode converter [26,27] to minimize the generation of stray radiation. The radius of the antenna waveguide launcher is slightly up-tapered towards the output by an angle of 4 mrad in order to avoid parasitic oscillations in this region. Due to the low fields along the edge of the helical cut, this advanced dimpled-wall launcher generates a well-focused Gaussian-like field pattern with low

edge-diffraction [28]. In combination with a three-mirror system the desired Gaussian output beam pattern is obtained, an example is shown in Fig. 12. The RF-field distribution was measured (perpendicular to the output RF-beam direction) at different positions with respect to the window. A Gaussian mode content of 97.5 % of the output beam was calculated from the measurements.

With the prototype gyrotrons in the TED-development line, two problems were faced: The specified output power of 1 MW was not completely achieved, which was attributed to an azimuthally inhomogeneous e-beam emission. Furthermore the pulse length was limited to about 15 minutes even at reduced power of 534 kW due to an increase of the internal gas pressure [29,30].

To eliminate these limitations, an improved quality assurance of the emitter ring (electron gun) was established before installing it into the gyrotron. To avoid the pulse length limitation due to pressure increase in the tube, external ion getter pumps were implemented in the design with improved RF stray radiation shielding. The R&D phase with TED was then terminated in 2002, followed by a commercial contract for 7 additional TED series gyrotrons. Together with both R&D-tubes and the CPI-gyrotron, all sockets of the ECRH-plant will be equipped.

All TED-gyrotrons are pre-tested in the FZK-test stand prior to shipment to IPP, where they undergo the final full performance test. The TED-gyrotron S.No.1 showed an almost linear dependence of output power versus beam current at constant magnetic field. The saturation in power as measured in the prototype was absent indicating the good emission of the cathode. An output power of 1 MW at 40 A and 1.15 MW at 50 A was measured in short pulse operation (ms). The corresponding efficiencies without depressed collector were 31 % and 30 %, respectively.

All gyrotrons under test show a frequency chirp of typically 200 MHz during the first couple of

seconds due to heating and expansion of the cavity. The optimisation of the operating parameters at high output power in 1 s-pulses was performed assuming that the instantaneous power is well described by the frequency difference between the initial frequency (cold cavity) and the instantaneous frequency (after one second). A slight power increase was measured while increasing the cavity field from 5.52 to 5.56 T. The maximum output power was achieved by adjusting the accelerating voltage (this corresponds to the energy of the electrons inside the cavity) confirming the law that the ratio between magnetic field and the relativistic factor  $\gamma$  has to be constant. Increasing the voltage beyond this value leads to an excitation of neighbouring modes. The measurements were performed at a constant beam current of 40 A, but with optimising the electron beam radius inside the cavity.

A strong dependence of the output power on the electron beam radius in the cavity was found. The desired mode can only be excited in a narrow range between 10.25 mm and 10.43 mm. At lower beam radii, arcing occurs, at higher radii a wrong mode is excited. The optimum value of the beam radius decreases slightly with decreasing cavity field and beam current.

In long pulse operation up to 3 minutes, which is the test stand limit at FZK for a beam current  $> 25$  A, the power was measured calorimetrically in an RF-load. The RF beam is directed and focused by two matching mirrors and two polarizers into the load, which is located at a distance of about 6 m from the gyrotron window. The polarizers generate a circularly polarized wave to homogenise the power loading on the surface of the load. The first matching mirror owns a grating surface, which directs a small amount of the RF beam towards a horn antenna with a diode detector to get a power proportional signal. The gyrotron was operated with a typical depression voltage in the range 25-30 kV to limit the collector loading and optimize the efficiency. Fig. 13 displays some gyrotron operating parameters for a pulse length of three minutes. The electron beam current  $I_{\text{beam}}$  drops somewhat at the beginning of the pulse due to beam emission cooling of the electron gun and recovers on a slow inherent timescale (10 -100

s) while boosting the heater power properly. The ion getter pump current (tube pressure) shows some changes also, but on a very low level. The increase of pressure is less than a factor of two reaching the  $10^{-9}$  mbar range. The highest measured directed power inside the load for a three-minute pulse was 906 kW. Including the external stray radiation, which was determined by calorimetric measurements inside the microwave chamber, the total gyrotron output power was 920 kW with an efficiency of 45 %. Thus the specified value of  $> 900$  kW for the power in the directed beam has been achieved.

After the successful tests at FZK, the tube was delivered to IPP Greifswald for final tests in 30 minutes operation and the year 2005 saw the successful full performance tests of gyrotrons from both manufacturers, CPI and TED at IPP. Fig.14 shows the TED gyrotron and SC-magnet in the installation at IPP-Greifswald.

Typical time traces of the output-power and the gyrotron pressure (GIP-current) for an experimental sequence of one short (5 min) and one longer pulse (30 min) are shown in Fig. 15 (top). The slow rise and fall times of the rf-power trace is determined by the characteristic time constant of the cw-calorimeter. A steady increase of the gyrotron pressure as seen from Fig. 15 (bottom), although at a very low level of a few  $\mu\text{A}$ , indicates, that the gyrotron has not yet reached steady state after 30 min, although all other measured parameters became stationary. Power modulation was demonstrated up to 20 kHz by modulating the body voltage. An almost linear dependence of the output power on the body voltage was measured. The rf-power vs. acceleration voltage characteristics is seen for the CPI-gyrotron in Fig. 16 (top) for 10 min pulses providing a very convenient voltage range for the power control.

An example for a beam-current scan is shown in Fig. 16 (bottom), each data point was taken in pulses with 1-5 min pulse duration. The scan was performed up to a maximum

output-power of 0.96 MW with an efficiency of 44 %, indicating the gyrotron capability. We have chosen somewhat more conservative parameters for the 30 min operation, which is the target operation time for W7-X. The gyrotrons were operated at a source power in the directed beam of about 0.9 MW (CPI) and 0.92 MW (TED), the related power measured in the calorimetric cw-load was 0.83 MW (CPI) and 0.87 MW (TED). Note, that due to the inherent mode filtering capability of a beam waveguide only the Gaussian mode content of the gyrotron beam reaches the cw-load. The total transmission losses after seven mirrors were estimated in the range 50-70 kW. As the beam parameters for the CPI-gyrotron were not known with the required accuracy, slightly higher losses (70 kW) resulting from an imperfect Beam-Matching-Optics unit (BMO) had to be accepted as compared to the TED-gyrotron (50 kW). The CPI-gyrotron opened a collector vacuum leak after having passed the acceptance test and was returned to the manufacturer for repair. The TED gyrotron S No. 1 was mothballed after the acceptance tests.

At present, 4 out of the 10 units of the ECRH-plant are operational and further commissioning is in progress. Although the TED gyrotron S.No. 2 failed to meet the required output power during the tests at FZK and will be returned to the manufacturer, series production is ahead of the limited test-and commissioning capability at FZK and IPP and the TED gyrotron S.No.3 is presently being prepared for the transfer to IPP for full performance tests. The measured Gaussian mode purity of the output beams of both TED-gyrotrons No. 2 and 3 is about 97 % and comparable to S.No. 1. The gyrotron S.No.4 is close to completion in the factory.

### **III.B The quasi-optical transmission system**

#### *III.B.1. The Multi-Beam-Waveguide Concept*

For high-power transmission of millimeter waves, free-space beam waveguides as well as highly oversized corrugated waveguides are used [31]. Owing to good experiences with a 800 kW / 140 GHz beam waveguide on the stellarator W7-AS, a quasi-optical transmission system was chosen for W7-X [32]. Here, the millimeter waves are transmitted as gaussian beam by iterative transformation with metallic mirrors [33,34]. The standard mirror design employs ellipsoids where the foci are determined by the phase centers of the incident and the reflected beam, respectively [35]. This shape gives minimum conversion to higher order modes [36]. Mirror shapes for astigmatic beams (as used for the matching of the gyrotron to the transmission line) are discussed in [37].

Main advantages of this technology are the low (ohmic and diffractive) losses, the high power capability due to relatively low field strength and the inherent mode filtering as high order modes are diffracted out of the system. A major disadvantage of beam waveguides is the diameter of the beam and thus the size of the mirrors governed by diffraction of the beams. Therefore systems with several channels are generally complex and bulky.

To overcome this disadvantage, a Multi-Beam Waveguide (MBWG) was developed for the ECRH transmission to W7-X. Here, many quasi-optical beams are transmitted by a common mirror system. Basically, the MBWG consists of four focusing mirrors in a confocal arrangement, and must simultaneously offer a low-loss propagation of all (on-axis and off-axis) beams in combination with a correct imaging of the beam positions from the input to the output plane. The principle is illustrated in Fig. 17, where one unit consisting of 2 mirrors in Z-configuration is sketched: At the input plane (located at a distance  $f$  in front of the first mirror), the waists of all beams are located, and the beams are injected parallel to each other into the common mirror system. Behind the first mirror, all beams cross in its focal plane. Behind the focal plane of the second mirror, the beams are parallel again, and the beam

configuration injected at the input is recovered. Additionally, for W7-X, the central (on-axis) beam will have a frequency of 70 GHz, which requires the full mirror surface due to the larger beam divergence at the longer wavelengths.

To optimise the mirror shapes and to find the best arrangement of the mirrors, diffraction calculations with Gaussian beam mode analysis were performed [38]. Note that for a compact MBWG design, the individual beams overlap on the mirrors, so that no optimisation of corresponding sections of the mirror surfaces is possible.

The study showed, that simple toroidal mirrors are the best compromise between the ellipsoidal shape required for optimum Gaussian beam transmission and the paraboloidal shape for best imaging characteristics. An essential parameter is the mirror arrangement: out of the 8 possible arrangements for the four mirrors, only two, the ‘Z-configuration’ and the ‘square configuration’ give optimum performance [38]. In the ‘square configuration’ four mirrors are arranged in a square with the reflecting surfaces pointing towards the centre of the square. Note, that additional plane mirrors have to be introduced to fit this arrangement into the transmission system. For both configurations, the spurious modes which are excited on each mirror surface destructively interfere after four mirrors, and the beams cross the output plane exactly perpendicular in the nominal position. For the parameters of W7-X, the matching coefficient between input and output is 99.9%. With the finite size of the mirrors taken into account, the transmission efficiency in the nominal mode is >99.5 %. Further calculations show, that even a much higher number of beams could be transmitted via a common mirror system without remarkable diffraction loss.

### *III.B.2. Design of the transmission system*

The general arrangement of the transmission system is sketched in Fig. 11. The gyrotrons,

which are installed behind the concrete walls of the underground beam duct radiate their power laterally through holes in the duct walls. For each gyrotron, a beam conditioning optics consisting of five single-beam mirrors is used. One Single Beam Waveguide (SBWG) module is shown in Fig. 18 together with additional components such as short-pulse calorimeter, rf-shielding elements and switch mirrors. The beam combining optics (BCO) module is also seen in the background. Two SBWG-mirrors (M1 and M2) match the gyrotron output to a Gaussian beam with the correct beam parameters. These mirrors are the only elements, which have to be adapted to the individual gyrotron output and can be designed and built according to the delivery sequence of the gyrotrons without affecting the lay-out of the overall system. The following two mirrors (P1 and P2) are corrugated with a sinusoidal corrugation [39] to set the polarisation needed for optimum absorption of the radiation in the plasma. The first of these polarizers (elliptical polarizer P1, groove period = 1.28 mm, depth = 0.56 mm), shifts the polarisation between the TE and the TM wave by  $90^\circ$ , thus by rotation any ellipticity of the reflected radiation can be set. The second polarizer (period = 1.28 mm, depth = 0.78 mm) has a corrugation for a  $180^\circ$  phase shift to turn the axis of the polarisation ellipse to the appropriate orientation. A fifth mirror (M3) directs the beam to a plane mirror array (BCO) at the input plane of the MBWG. This MBWG is designed to transmit up to seven beams (five 140 GHz beams, one 70 GHz beam plus an additional spare channel) from the gyrotron area (input plane) to the stellarator (output plane). In addition to the four focusing mirrors, three additional plane mirrors are used to fit the transmission lines into the building. A section of the two symmetrically arranged MBWG's is shown in Fig. 19.

Two towers house the mirror array (Beam Distribution Optics, BDO-module) at the output plane of the MBWGs, which separates the beams and directs them via two mirrors towards the plug-in Launcher as shown in Fig. 20. The spare channel of the MBWGs is used to switch one beam on each side from a standard LFS launcher to a HFS launcher in the N-port

(see Sec. II.D). The length of the MBWGs is 45 m, the total length of the transmission lines is 57 to 65 m depending on the location of the gyrotron.

### *III.B.3. Diagnostics for the transmission system*

Power monitoring in the line is performed with grating couplers [40], which are embedded into the copper surface of M1. The coupled beam is either transmitted to a matched horn or a bolometer. M1 is also equipped with temperature sensors and a flow meter for calorimetric measurement of the ohmic loss on the mirror to monitor the transmitted power. By switching the mirror SC (see Fig. 18) each gyrotron beam can be directed into the calorimetric load consisting of a double-walled cylindrical absorbing chamber with two layers of water-cooled Teflon hoses at the inner wall. An optimized conical mirror distributes the radiation homogeneously over the Teflon hoses, a modified Winston cone [41] at the input maximizes the throughput of the incoming radiation through the 50 mm diameter aperture and reduces the reflections to about 1 %. The calorimeters are designed for a pulse duration of about 0.5 s at full power.

By tilting one of the BCO mirrors, the corresponding beam can be steered via mirror MD into a commercial cw load (see Fig. 19). As this load showed reflections of the order of several percent, a mirror with the shape of a rotational ellipsoid was attached at the input of the load, which reduces the reflected power significantly.

### *III.B.4. Mirror technology*

All mirrors must maintain a stable surface under the heat loads imposed by the ohmic loss of the millimetre waves. The ohmic loss of different copper surfaces as used in the transmission line (plane; shallow diagnostic gratings; polarising grooves) was measured with a 3-mirror

resonator technique [42], the data were used as input for the mirror design and cooling concept. This results in losses of up to 3 kW per Megawatt beam with thermal loads of up to  $100 \text{ W/cm}^2$  on each mirror surface.

To minimise surface deformations due to thermal loads a 60 – 70 mm thick honeycomb structure from stainless steel with a thin (2 mm) layer of electro-formed copper on the mirror surface was chosen as seen from Fig.21. The cooling channels are in direct contact with the copper layer and spiral from the centre (water inlet) to the edge of the mirror (water outlet(s)).

The width, the depth, and the number of the spirals is adapted to the different mirror shapes (rectangular, square, hexagon, circular) and dimensions (190 x 270 mm .... 740 x 1100 mm). The heat removal matches the local heat transfer to the Gaussian distribution of the heat load [43]. Even in the transient phase in the first minute after full power switch-on, the variation of the mirror curvature stays below  $10^{-3} \text{ m}^{-1}$ , which was confirmed experimentally. All mirrors are mounted on stable supports allowing two-axis adjustment by remote control.

### *III.B.5. Alignment of the mirror system*

The mirrors are pre-aligned with lasers, final alignment is performed with the high-power beams using thermographic methods. If necessary, the alignment will be continuously checked by a system based on FM-reflectometry [44]. For this purpose, all mirrors have shallow phase gratings on their surface designed such that for correct alignment the -1<sup>st</sup>-order Littrow condition is fulfilled at a frequency of 188 GHz. A low-power probing beam at this frequency which is coupled co-axially into the system will lead to reflected signals from the mirrors which are a measure for the quality of the alignment of the mirrors. A test of this scheme at the quasi-

optical part of a 140 GHz ECRH transmission line on W7-AS was successful and showed a spatial resolution of 0.15 m, which is by far enough to discriminate signals from the individual mirrors.

As alternative for the alignment control and power measurement in front of the torus window, a system based on a holographic grating coupler with conical scanning of the diffracted beam is in preparation [45].

### **III.C. Transmission characteristics**

#### *III.C.1 Transmission efficiency and mode purity*

The overall transmission efficiency is determined by ohmic dissipation in the mirrors, diffraction loss due to mode conversion and mirror surface deformation, beam truncation of the reflectors and windows, misalignment, as well as atmospheric absorption. The estimated contributions are listed in Table III. One can see, that a total transmission efficiency of 90 % is expected for a pure gaussian beam. Additionally, higher-order mode losses from the gyrotron output beam of typically 3 % are estimated. Stray radiation arising from diffraction losses inside the gyrotron of the order of 5 % has to be absorbed by water-cooled absorbers and the concrete walls of the beam duct.

#### *III.C.2 Low-power measurements of transmission efficiency and mode purity*

Due to the complexity of the system and in order to test its over-all performance and stability, a full-scale prototype had been built. Amplitude and phase measurements of the beams have been performed at the characteristic planes using various field scanning devices together with a vector network analyzer. An example of the beam power and phase

distributions for all transmission channels at the output plane of the MBWG (corresponds to the position of the BDO, see Fig. 11) is shown in Fig. 22. For each channel, the patterns show an almost rotationally symmetric amplitude distribution and only small variations of the phase and thus demonstrate the good imaging characteristics of the confocal system even for off-axis beams. The mode analysis of the measured beam patterns at the exit of the multi-beam section yields a TEM<sub>00</sub>-mode purity of  $\geq 98\%$ . The total transmission efficiency of the prototype system (17 mirrors) was checked by calorimetric methods and yielded  $90\pm 2\%$ , which is in good agreement with the theoretical value.

### *III.C.3 High-power measurements of beam parameters*

The thermographic recording, phase retrieval and mode analysis of the output beams of several gyrotrons yielded a high TEM<sub>00</sub> mode purity of  $> 95\%$ . Therefore, the matching mirrors M1 and M2 were designed as simple ellipsoidal mirrors, which only have to correct for the slight astigmatism of the gyrotron beam. At the end of the single-beam line in front of the dummy load (see Fig. 19), the intensity distribution of the beam was measured at several positions using thermography of a PVC target inserted into the beam path. The preliminary analysis of the data is plotted in Fig. 23, with the insert showing a typical beam pattern. As can be seen from the graph, the beam radii in vertical and horizontal direction are in good agreement with the calculated parameters of the circular Gaussian beam.

### **III. D. Integrated high-power, cw tests**

The full performance tests were performed with both, the TED and the CPI gyrotron operating at an output power of about 0.9 MW for 30 minutes. The microwave beams were

transmitted through 7 single beam mirrors of the transmission system into a calorimetric cw-load to perform integrated tests of two modules of the ECRH plant. The data for cw-operation as presented in Sec. III.A were obtained in this set-up.

During high-power tests all mirrors performed well. In particular, no arcing was seen on the corrugated surfaces of the polarizers, which are considered the most critical (and most loaded) elements, provided that they were clean.

It is worth noting, that all peripheral systems at IPP like main power supply, central cooling system, body-modulator, transmission line components, RF-diagnostics, as well as the central control and data-acquisition system are new and had to go through this integrated qualification process together with the gyrotron.

Small side lobes of the rf-beam were hitting the beam duct concrete wall or weakly cooled elements like the first mirror-support and additional water cooled absorbing targets had to be installed at the measured hot spots to avoid overheating. It is expected, that some fraction of the lost power from the CPI-gyrotron will be recovered by an improved BMO, which would increase the useful power in the Gaussian mode. More important, however, is the reduction of the power in the beam side-lobes, which is already very small. Even a small fraction of directed power (some kW), which does not hit the water cooled transmission mirrors, may create hot spots and damage of weakly cooled surfaces in cw-operation. The more or less isotropic deposition of the small fraction of stray radiation is easily handled by the concrete walls and is of minor concern.

With the encouraging results from the integrated tests of two modules, series production and commissioning of the major system components was released and 4 modules are completed meanwhile.

The high-power, full performance, cw tests reported here were restricted to the SBWG-section of the transmission line. For tests of the full distance transmission including the

MBWG-section, a special optical arrangement with retro-reflectors mounted in the first image plane of the MBWG (i.e. at half distance of the MBWG (see Fig. 11)) is being prepared. This is a necessary intermediate step, because the optical elements in the torus hall can be installed and tested only in a late phase of the W7-X-torus assembly.

As seen from Fig. 24, the retro-reflector is mounted on rails and on a turntable to reflect either one of the six beams, which are propagating forward in an outer channel of the MBWG, backward via the central channel. An additional movable mirror near to the entrance plane of the MBWG focuses the beam (also via mirror MD) into the cw load.

The ECRH-system served already as a high power test bed for ITER ECRH- components, which were developed at different laboratories under EFDA umbrella. The open transmission system, which allows an easy implementation of different test arrangements in the existing transmission system, turned out to be the key-feature for fast and efficient test-programs: The mock-up version of a remote steering launcher, which is an option for the ITER upper launcher, was tested under high power conditions at IPP-Greifswald [46,47]. High power, short pulse tests of a mock-up version of a 2 MW calorimetric load were also successfully performed recently.

#### **IV FRONT-STEERING LAUNCHER AND IN-VESSEL COMPONENTS**

The ECRH and ECCD scenarios as discussed in Sec. 2 require a flexible launching system to cope with the demands for different mode-coupling. Furthermore, the high heat load conditions in cw-operation necessitate a reliable technical solution for the in-vessel components, which can sustain both, the power load of the microwaves and the plasma radiation. Several critical components have already been tested with respect to reliability and heat loading capability.

#### IV.A ECRH front steering launcher development

Altogether 12 RF-beams (10 plus two spare) will be launched through 4 large equatorial ports (type A and E) for the LFS-launch scenarios. Three beam-lines are stacked and incorporated into one plug-in launcher (PILA) as shown in Fig. 25 (top). Two out of the ten beam lines can be switched towards two lateral N-type ports for the HFS scenarios. Each of the equatorial beams is quasi-optically transmitted through its individual synthetic diamond vacuum window towards a fixed focusing mirror and a bi-axially movable, plane steering mirror at the front end. Water-cooled tubular structures are screening the beams and serve as a rigid mechanical support for the front mirrors. Specially designed apertures inside the beam tubes reduce backward transmission of reflected power. The movable mirrors enable a poloidal steering range of  $\pm 25^\circ$  and a toroidal steering range between  $\pm 15^\circ$  and  $\mp 35^\circ$ , which is more demanding than the present ITER design. The cooling water of the front steering mirror is feed through two push-pull rods, which are used for the mirror positioning. The joints of the push-pull rod system are bridged by tube spirals as shown in Fig. 25 (bottom). The joints are screened by additional copper half shells and the surrounding tube spirals against microwave and plasma radiation. Assumed parameters for the design are a microwave radiation level of about  $500 \text{ kW/m}^2$  and a plasma radiation of  $100 \text{ kW/m}^2$ . A launcher mock-up was build, which incorporates the most critical elements in original size, and mechanical tests were performed with respect to the push-pull rod positioning accuracy and the motor-drive reliability. In a test with 10000 full scan cycles the accuracy of the positioning was found to be  $0.05^\circ$ . The motor drive was also successfully tested in a magnetic field of up to 40 mT, which is expected at the final motor position near the stellarator. The most critical elements are the tube spirals made of stainless steel tubes with 7 and 8 mm diameter and 1 mm wall thickness. Due to the bi-axial mirror movement, they

have to withstand both a bending angle of up to  $45^\circ$  and a torsion of  $10^\circ$ . The maximum tension was calculated by an analytic model, which was benchmarked by a cyclic test of a down-scaled spiral (reduced number of windings). Cyclic tests with 10000 cycles were performed with increasing bending angle until the critical tension was reached and the spiral was broken. Based on these results the spirals were designed with a safety margin of about two. They passed the 10000 –cycle, full range test successfully. The spirals were annealed to minimize the internal tension before assembly. For two types of the spirals the tube circular cross-section was optimized and pressed into an elliptical one to avoid the contact of neighboring winding at the maximum bending angle. The measured hydro-mechanical properties of the spirals require a water-cooling system with 16 bar pressure for the front mirror cooling. After the successful completion of the R&D for the rod-joint-spiral assembly, the parts were integrated into the mock-up launcher including all vacuum feed-through's for the water cooling, motor drive rods etc. and are presently being tested in a special Microwave Stray Radiation Loading (MISTRAL) test facility.

The O2, X3 and OXB scenarios feature a high microwave stray radiation level inside the vacuum vessel of W7-X originating from the non-absorbed power, which is distributed by multiple reflections. The stray radiation was modeled with a multi resonator model [48], which was benchmarked with measurements at the FTU-Tokamak and the W7-AS stellarator. We expect a stray radiation level of  $500 \text{ kW/m}^2$  in the antenna ports and  $200 \text{ kW/m}^2$  in the W7-X torus modules No.1 and 5, where the ECRH is launched. The high stray radiation level could thermally overload insufficiently cooled in-vessel components (first wall, diagnostics, divertor etc.) and generate sparks in wavelength resonant structures. The MISTRAL-facility as shown in Fig. 26 (left) was build, therefore, for integrated tests of all critical W7-X in-vessel components under vacuum-conditions and in presence of an rf-stray-radiation background. The level of the background radiation is adjusted to simulate the W7-

X conditions under cw, ECR-heating. The MISTRAL facility is presently powered with an average, cw-power of 30 kW at 140 GHz, which corresponds to the expected background radiation in W7-X. The test facility and the scheme of stray radiation generation is shown in Fig. 26 (right). The chamber has Al-walls with high reflectivity and a rough inner surface, which, in combination with a special feeder antenna system, generates a homogenous and isotropic background radiation in the centre of the vessel (shaded area). The microwave beam is reflected from the chamber walls like a ‘whispering gallery mode’ in a waveguide and every reflection at the rough in-vessel surface illuminates the shadowed central test volume. The rf-field distribution in the chamber was measured and shows a homogenous and isotropic central volume in agreement with the modeling.

The MISTRAL-facility is equipped with a set of standard size vacuum ports, which are used in the W7-X vacuum vessel, and one of the large, elongated A-ports. This port can house the complete ECRH plug-in launcher for integrated tests.

For the N-type port launch no detailed design exists at present, but a remote steering launcher may be an attractive option

#### **IV.B In vessel structures**

For the O2 and X3 ECRH scenarios, where the incident beams are not completely absorbed in the first path, microwave reflectors have to be installed at the inner vessel wall opposite to the steering mirrors. The beam is reflected at an optimum angle to maintain a well-defined second path absorption in the plasma. Furthermore these reflectors prevent overheating of the vessel wall in cw-operation. The exact position was determined by ray-tracing calculations as seen from Fig. 27, (left). These metallic tiles are integrated in the graphite armour of the plasma-facing first wall and consist of a TZM mirror surface, which is

clamped on a water-cooled copper structure. An array of pick-up horns for the measurement of the transmitted beam profile and beam power incident on the mirror is incorporated into each of the tiles. The thermal properties were simulated for different beam profiles. Assuming an incident microwave power of 0.5 MW, which corresponds to 50 % single pass absorption, and a beam waist from ray tracing of 20 mm, the tile temperature reaches typically 300° C, which is acceptable. A test tile has been manufactured and is being prepared for high power test.

## **V. SUMMARY AND CONCLUSIONS**

The ECRH-system for W7-X is the most ambitious and largest cw-plant presently under construction, its relevance for ITER is obvious. The operation scenarios with ECRH only will cover the full density range for plasma operation. In addition the X3 heating provides an operation at a reduced magnetic field of 1.7 T. The exploration of the  $\beta$ -limits of W7-X, however, requires significantly higher heating power and reduced magnetic field. This will be explored with NBI, which is foreseen in the final stage with 20 MW. Nevertheless remarkable  $\beta$ -values are predicted already with ECRH alone, depending on the assumed heat-transport coefficients. The in-vessel components for W7-X are designed to provide cw operation for all ECRH scenarios. Intensive prototype tests have been performed in order to build a highly reliable system.

The successful full performance cw-tests of two out of 10 ECRH-modules have proven that the ECRH-system is based on a viable and robust design. The R&D phase for the gyrotrons and the transmission line was terminated and series production, installation and commissioning is in progress. The modular concept proved to be essential for the project realization, which runs on time and budget. MW-class cw-gyrotrons at the required

frequency are now commercially available from two industrial manufacturers. The quasi-optical multi-beam waveguide system offers favorable transmission characteristics close to the theoretical predictions and the most loaded components showed an excellent performance under full power, cw conditions.

The test results and the operational experience may provide valuable input for the ITER-ECRH system, because the physics demands and the main system parameters are comparable, while keeping in mind, that the ITER-system must satisfy additional requirements such as operation and maintenance in a radioactive environment.

### **Acknowledgment**

The authors wish to thank the technical staff at FZK, IPF and IPP for their excellent contributions in solving numerous technological problems during the R&D of the sophisticated ECRH-components. We are grateful to the key persons at TED and CPI for their great effort and their readiness to incorporate innovative concepts in the Gyrotron-R&D. Finally we would like to thank all partners in the collaborating research laboratories for their stimulating discussions and active support.

## References:

- [1] V. ERCKMANN, H.J. HARTFUß, M. KICK, H. RENNER, et al.:  
*Proc. 17th IEEE/NPSS Symposium on Fusion Engineering, San Diego, USA (1997).*  
*Ed. IEEE, Piscataway, NJ 1998, 40 - 48*
- [2] M. ROME', V. ERCKMANN, U. GASPARINO, N. KARULIN :  
*Plasma Phys. Control. Fusion* **40** (1998) 511-530
- [3] H. P. LAQUA, V. ERCKMANN, H.J. HARTFUß, H. LAQUA, W7-AS TEAM, AND  
ECRH GROUP, *Phys. Rev. Lett.* **78**, 3467 (1997)
- [4] E. WESTERHOF, *Plasma Phys. Control. Fusion* **39** (1997) 1015
- [5] M.D. TOKMAN, E. WESTERHOF AND M.A. GAVRILOVA:  
*Plasma Phys. Control. Fusion* **42** (2000) 91
- [6] M. TAGUCHI, *Plasma Phys. Control. Fusion* **31** (1989) 241
- [7] F. VOLPE, *PhD Thesis*, University of Greifswald, Germany (2003)
- [8] S. HIRSHMAN AND J. Whitson, *Phys. Fluids*, **26** (1983) 3553
- [9] E. POLI, A. PEETERS, G.V. PEREVERZEV, *Comp. Phys. Commun.* **136** (2001) 90
- [10] M.A. BALAKINA, M.D. TOKMAN , O.B. SMOLYAKOVA:  
*Plasma Physics Reports* **29** (2003) 53
- [11] YU. TURKIN, H. MAASSBERG, C. D. BEIDLER, J. GEIGER et al.,  
*Fusion Sci. Technol.*, **50** (2006) 397
- [12] U. STROTH, M. MURAKAMI, R.A. DORY, H. YAMADA, S. OKAMURA, F.  
SANO, T. OBIKI: *Nucl. Fusion* **36** (1996) 1063
- [13] H. MAAßBERG, C.D. BEIDLER, U. GASPARINO, M. ROME', et al.  
*Phys. Plasmas* **7**, 295 (2000)

- [14] W.I. VAN RIJ AND S.P. HIRSHMAN, *Phys. Fluids B* 1 563(1989)
- [15] H. MAASSBERG, R. BRAKEL, R. BURHENN, U. GASPARINO et al.,  
*Plasma Phys. Control. Fusion* **35**, (1993) B319
- [16] K. MCCORMICK, P. GRIGULL, R. BURHENN, R. BRAKEL, et al.:  
*Phys. Rev. Letters* 89 (2002) 1131
- [17] P.GRIGULL et al. *Plasma Phys. Control. Fusion* 43 (2001) A175
- [18] H.P. LAQUA et al, *Plasma Phys. Control. Fusion* **41** (1999) A273
- [19] A. WELLER, J. GEIGER, M. ZARNSTORFF, E. SALLANDER, et al.,  
*Plasma Phys. Contr. Fusion* 45 (2003) A285-A308
- [20] L. GIANNONE, R. BURHENN, K. MCCORMICK, R. BRAKEL, Y. FENG, P.  
GRIGULL, Y. IGITKHANOV, NBI TEAM, ECRH TEAM AND THE W7-AS  
TEAM:  
*Plasma Phys. Control. Fusion*, **44**, 2149 (2002).
- [21] R. HEIDINGER, G. DAMMERTZ, A. MAIER, AND M. THUMM:  
*IEEE Trans. Plasma Sci.*, **30**, pp. 800-807, 2002.
- [22] G. DAMMERTZ, S. ALBERTI, A. ARNOLD, E. BORIE, et al.,  
*IEEE Trans. Plasma Science* 30 (2002) 808-818
- [23] K. FELCH, M. BLANK, P. BORCHARD, P. CAHALAN, S. CAUFFMAN, T.S.  
CHU AND H. JORY, *Proc. Joint 30th Int. Conf. Infrared and Millimeter Waves & 13  
Int. Conf. Terahertz Electronics*, pp. 237-238, (2005).
- [24] K. FELCH, M. BLANK, P. BORCHARD, P. CAHALAN, S. CAUFFMAN, T.S.  
CHU AND H. JORY, *Journal of Physics: Conference Series* 25 (2005) pp. 13-23.
- [25] H. JORY, M. BLANK, P. BORCHARD, P. CALAHAN, S. CAUFFMAN, T.S. CHU,  
K. FELCH: *High Energy Density and High Power RF: 6<sup>th</sup> Workshop, Berkely Springs,  
USA*, ed. S.H. Gold and G.S. Nusinovich, (2003), *AIP Conf. Proc.* **691**, p.224

- [26] G.G. DENISOV, A.N. KUFTIN, V.I. MALYGIN, N.P. VENEDIKTOV, D.V. VINOGRADOV, AND V.E. ZAPEVALOV: *Int. J. Electronics*, vol. 72, pp. 1079-1091, 1992.
- [27] S.N. VLASOV, L.I. ZAGRYADSKAYA, AND M.I. PETELIN,  
*Radio Eng. and Electron Physics*, vol. 20, pp. 14-17, 1975.
- [28] M. THUMM, X. YANG, A. ARNOLD, G. MICHEL, J. PRETTEREBNER,  
D.WAGNER: *IEEE Trans. on Electron Devices*, **52**, no. 5, pp. 818-824, 2005.
- [29] G. DAMMERTZ, S. ALBERTI, A. ARNOLD, D. BARIOU, et al.:  
*IEEE Trans. Plasma. Sci.*, **52**, no. 5, pp. 808-814, 2005.
- [30] G. DAMMERTZ, S. ALBERTI, A. ARNOLD, D. BARIOU, et al.:  
*IEEE Trans. Plasma. Sci.*, **34**, no. 2, pp. 173-186, 2006.
- [31] THUMM, M. and KASPAREK, W.:  
*Fusion Eng. Design* 26 (1995) 291 – 317
- [32] W. KASPAREK, H. KUMRIC, G.A. MÜLLER, P.G. SCHÜLLER, V. ERCKMANN:  
*High power microwave generation and applications*, D. Akulina, E. Sidoni and C. Wharton, eds., *Societa Italiana di Fisica*, ISBN 88-7794-044-1, Bologna 1992
- [33] EMPACHER, L., FÖRSTER, W., GANTENBEIN, G., KASPAREK, W., et al.:  
*Fusion Technology 1996*, Amsterdam: Elsevier Science B.V. 1997, 541-544.
- [34] GRAU, W. in Kleen, W. and Müller, R.: *Laser*. Berlin: Springer 1969.
- [35] GOLDSMITH, P.F.: *Quasi-optical Systems*. New York: IEEE Press, Chapman and Hall, Publishers, ISBN 0-7803-3439-6, 1998
- [36] MURPHY, J.A.: *Int. J. Infrared Millimeter Waves* 8 (1987) 1165 – 1187
- [37] VINOGRADOV, D.: *Int. J. Infrared Millimeter Waves* 16 (1995) 1945 – 1963
- [38] EMPACHER, L. and W. KASPAREK, W.:  
*IEEE Trans. Antennas Propagat.*, vol. AP-49 (2001) 483 – 493

- [39] KOPP, K.W.; KASPAREK, W.; HOLZHAUER, E.:  
*Int. J. Infrared Millimeter Waves* **13** (1992) 1619 – 1631
- [40] L. EMPACHER, W. FÖRSTER, G. GANTENBEIN, W. KASPAREK, H. KUMRIC,  
G.A. MÜLLER, P.G. SCHÜLLER, K. SCHWÖRER, AND D. WAGNER et al.:  
*Proc. 20<sup>th</sup> Int. Conf. on Infrared and Millimeter Waves, Lake Buena Vista, Orlando*  
*(1995) 473 - 474.*
- [41] WINSTON, R.: *J. Opt. Soc. Amer.* **60**, 245-247, 1970.
- [42] KASPAREK, W., A. FERNANDEZ, F. HOLLMANN, and R. WACKER:  
*Int. J. Infrared and Millimeter Waves* **22** (2001) 1695-1707.
- [43] H. HAILER, G. DAMMERTZ, V. ERCKMANN, G. GANTENBEIN,  
F. HOLLMANN, W. KASPAREK, W. LEONHARDT, M. SCHMID, P.G.  
SCHÜLLER, M. THUMM, M. WEISSGERBER:  
*Fusion Eng. Des.* **66-68** (2003), 639 – 644.
- [44] EMPACHER, L., FÖRSTER, W., GANTENBEIN, G., KASPAREK, W., KUMRIC,  
H., MÜLLER, G.A., SCHÜLLER, P.G., SCHWÖRER, K., SCHUMACHER, U.,  
WAGNER, D. and ZOHN, H.: *Proceedings of the 10th Joint Workshop on ECE and*  
*ECRH, ed. T. Donne and A.G.A. Verhoeven, Singapore: World Scientific 1997, 561-568.*
- [45] J. SHI AND W. KASPAREK:  
*IEEE Trans. Antennas Propagat.* **AP-52** (2004) 2517 – 2524.
- [46] B. PLAUM, G. GANTENBEIN, W. KASPAREK, K. SCHWÖRER, M GRÜNERT,  
H. BRAUNE, V. ERCKMANN, F. HOLLMANN, L. JONITZ, H.P. LAQUA,  
G. MICHEL, F. NOKE, F. PURPS, A. BRUSCHI, S. CIRANT, F. GANDINI, A.G.A.  
VERHOEVEN, ECRH GROUPS AT IPP GREIFSWALD, FZK KARLSRUHE AND  
IPF STUTTGART: *Fusion Sci. and Tech.* **50** (2006) 1–14.

- [47] B. PLAUM, G. GANTENBEIN, W. KASPAREK, K. SCHWÖRER, et al.:  
*J. Phys.: Conf. Ser.* 25 (2005) 120-129
- [48] H.P. LAQUA, V.ERCKMANN, M. HIRSCH, W7-AS TEAM, F. GANDINI:  
*Proc. 28<sup>th</sup> EPS Conf. Control. Fusion and Plasma Phys., Funchal 2001, (Eds.) C. Silva, C. Varandas, D. Campbell, ECA 25A, European Physical Society, Geneva 2001, 1277-1280.*

## Figure Captions:

- Figure 1:** The W7-X Stellarator
- Figure 2:** Density range for different heating scenarios at W7-X
- Figure 3:** Top: Central electron temperature  $T_e(0)$  as a function of density for different heating power: hatched area are the temperature and density diagram based on the ISS95 confinement scaling [12], the curves are results based on neoclassical confinement approach. Bottom: radial profiles of the electron heat diffusivity: dotted curve from [12]; solid and dashed curves are the neoclassical and anomalous contributions from [11],  $r_{eff}$  is the effective plasma radius.
- Figure 4:** Plasma profiles with 4MW of ECRH: (a) the electron density (solid curve) and ECRH power deposition profile (dashed curve); (b) the electron (solid curve) and ion (dashed curve) temperatures; (c) the radial electric field.
- Figure 5:** Single pass absorption for the O2-mode (left, squares)) and the X3-mode (right, squares)) as a function of density. The central temperature (circles) was calculated for an input power of 10 MW.
- Figure 6:** Magnetic field configuration and microwave-beam path from ray-tracing calculations for the X3-mode. Left: Poloidal plane, Right: equatorial plane.
- Figure 7:** (a) Ray trajectories for O2-mode for HFS launch in the ‘triangular plane’. The resonance line ( $B = 2.5$  T) is also shown. (b) Deposition profiles for both trapped (dashed line) and passing electrons (dashed dotted line) and the total one (solid line). (c) Integral absorbed powers (notations are the same as in (b)).

- Figure 8:** (a) The ray trajectory in the equatorial plane. (b) Evolution of  $N_{\perp}$  and  $N_{\parallel}$ , as well as evolution of  $k v_{gr} / (k v_{gr'})$  along the ray path (c).
- Figure 9:** Current drive efficiency  $J/P$  as a function of the launch angle  $\phi$  for the X2-mode at different densities.  $J$  is the total current and  $P$  is the RF-power.
- Figure 10:** Volume averaged plasma- $\beta$  at the density limit as a function of the absorbed power for different heating scenarios: the solid and dashed curves are the  $\beta$ -limit predictions based on the improved ISS95-energy confinement time scaling for the X2/O2 and X3 heating, respectively; the solid and dashed curves marked by circles are the same curves, but based on the energy confinement time derived from [11].
- Figure 11:** Schematic design of the 140 GHz/10 MW ECRH-plant for W7-X  
a) cross section b) top view
- Figure 12:** Thermographic images of the RF-beam (power distribution) at different distances from the gyrotron window (from the left: 1282 mm, 1082 mm, 882 mm and 682 mm). The target size is 167 mm x 167 mm, the maximum temperature increase is 21.8, 21.8, 24, and 33.8 °C, respectively. Neighboring colors are separated by 10 % of the maximum temperature increase.
- Figure 13:** Operation parameters vs. time for the TED gyrotron S.No.1 in 3 min pulse duration. From top to bottom: accelerating voltage ( $U_{acc}$ ), beam current ( $I_{beam}$ ), body voltage ( $U_{Body}$ ), cathode voltage ( $U_{cath}$ ), diode signal ( $U_{diode}$ ) and pressure monitor (vacuum). All quantities are displayed in arb. units with linear scale.
- Figure 14:** The TED SNo.1-Gyrotron at IPP.

- Figure 15:** Example of a 30 min shot for the TED gyrotron S.No.1 (with a 5 min shot as precursor). RF-power (top) and gyrotron vacuum (GIP-current, bottom) as a function of time (h,min,sec).
- Figure 16:** Top: Output power (squares) and RF-power to load (dots) as a function of the acceleration voltage (CPI-Gyrotron). Bottom: Same quantities as a function of the beam current for the TED Gyrotron S.No.1.
- Figure 17:** Principle set up of a confocal 2-mirror multi-beam waveguide (Z-configuration).
- Figure 18:** Beam conditioning unit of channel B5 consisting of matching mirrors M1 and M2, Polarizers P1 and P2, as well as a calorimeter C with switching mirror SC. Stray radiation absorbers (AB1) are mounted behind M1 and inside the wall bore hole. M3 (not shown) guides the beam to the beam combining optics BCO. Mirrors SEN1 and SEN2 allow to switch the beam to transmission channel N serving the N-port for HFS launch.
- Figure 19:** View into the transmission duct showing mirrors M6, M7 of the two MBWGs (foreground) and the MBWG mirrors M5 as well as mirrors MD, which allows to transmit each individual beam into a calorimetric CW load (background).
- Figure 20:** Top: One of the ECRH towers, which houses the BDO-module. Bottom: Detail of the mirror-array in front of the equatorial ports. The mirror for HFS-launch through a separate N-port is also seen.
- Figure 21:** Single beam mirror with the Cu-SS sandwich structure. The copper surface is partly removed to show the cooling channel.
- Figure 22:** Low-power measurements of power density (left) and phase distribution (right) for seven beams at the output plane of the MBWG. Scale: 3 dB/color

step, 20°/colour step. The area of each measurement plane is 200 mm x 200 mm.

**Figure 23:** Beam radii in horizontal (measurement: dots; fit: solid line) and vertical (measurement: squares, fit: dotted line) direction of the beam in front of the dummy load as deduced from thermographic images (see insert), and comparison with design (dashed line).

**Figure 24:** Retro-reflector mounted in the beam duct. The direction of the incident and reflected beam is indicated, the axis of symmetry (dashed dotted line) and the rotation direction is also sketched.

**Figure 25:** ECRH plug-in launcher for the equatorial port in W7-X. Top: inside port design. Bottom: Mirror drive with water-cooling spirals for the front mirror.

**Figure 26:** Left: The MISTRAL-facility. Several W7-X standard ports are seen together with a large W7-X equatorial port (A-type) in front. Right: Scheme of stray radiation generation.

**Figure 27:** Left: Ray-tracing calculation for the optimum position of the O2 and X3 reflector tiles at the in-board side of the plasma vessel. Right: Heat load simulation of a strongly focused ECRH- beam (500 kW, beam waist 20 mm) at the TZM-reflector tile.

Figure 1

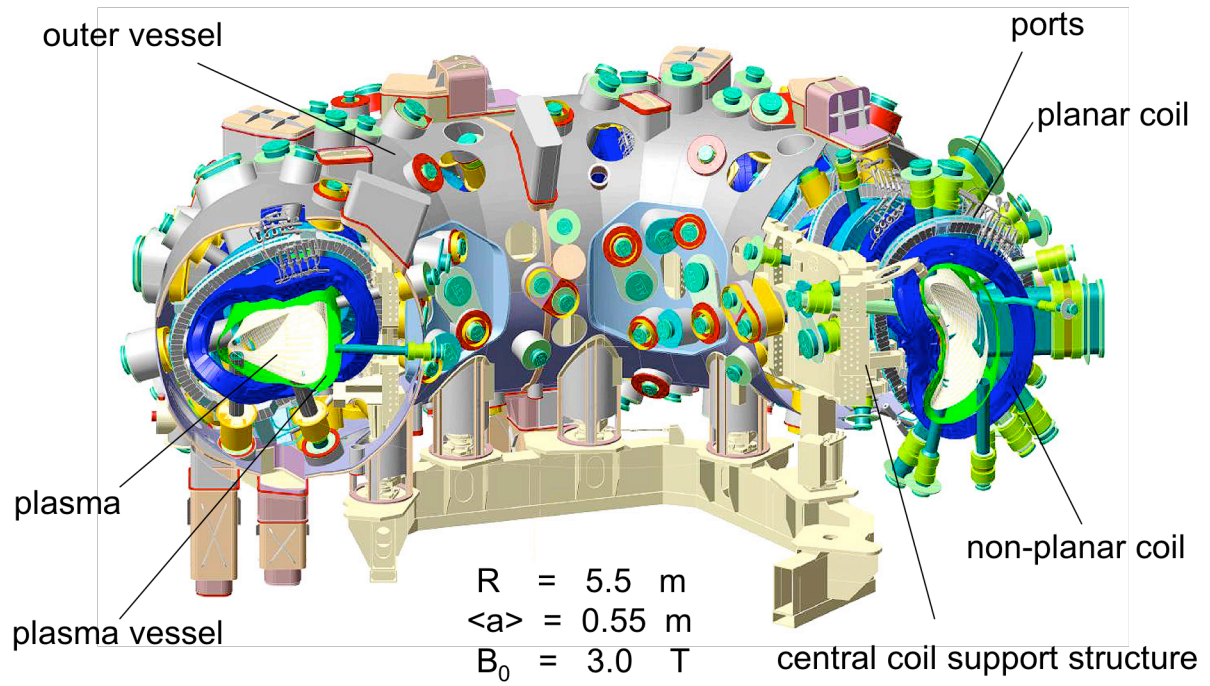
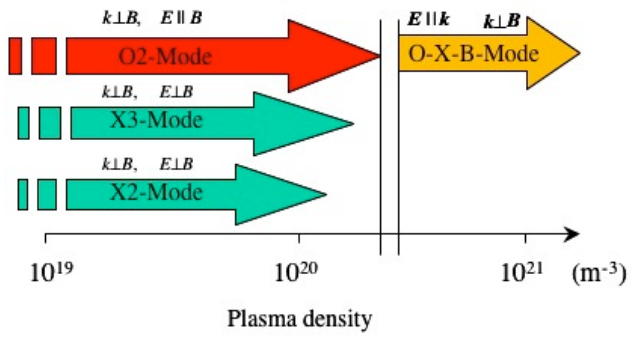
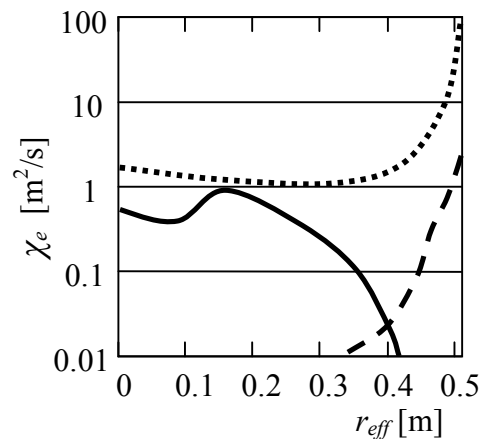
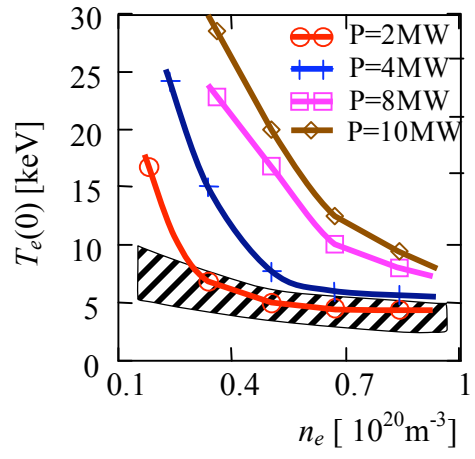


Figure 2



**Figure 3**



**Figure 4**

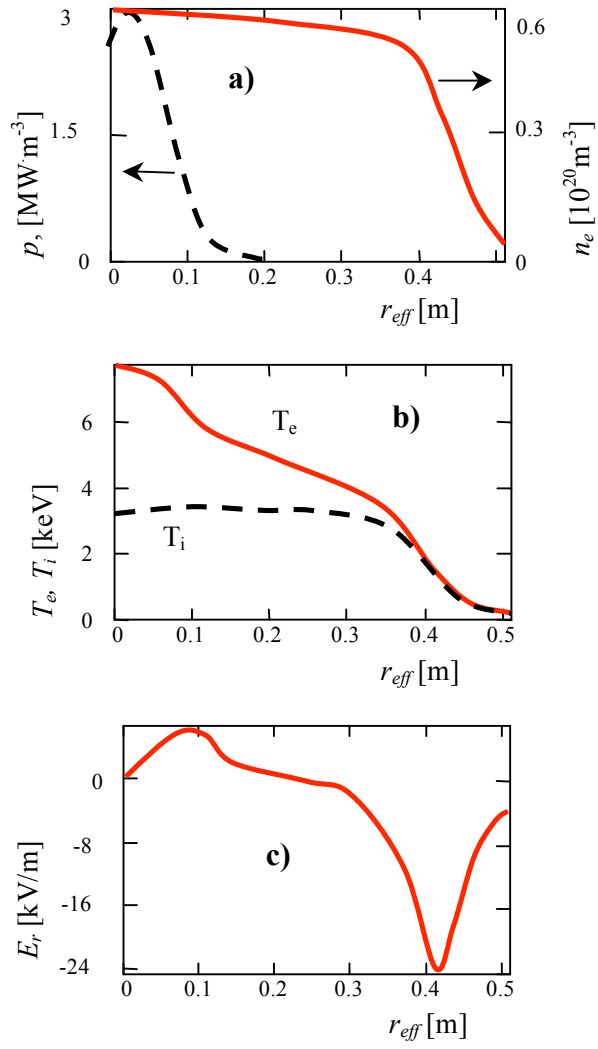
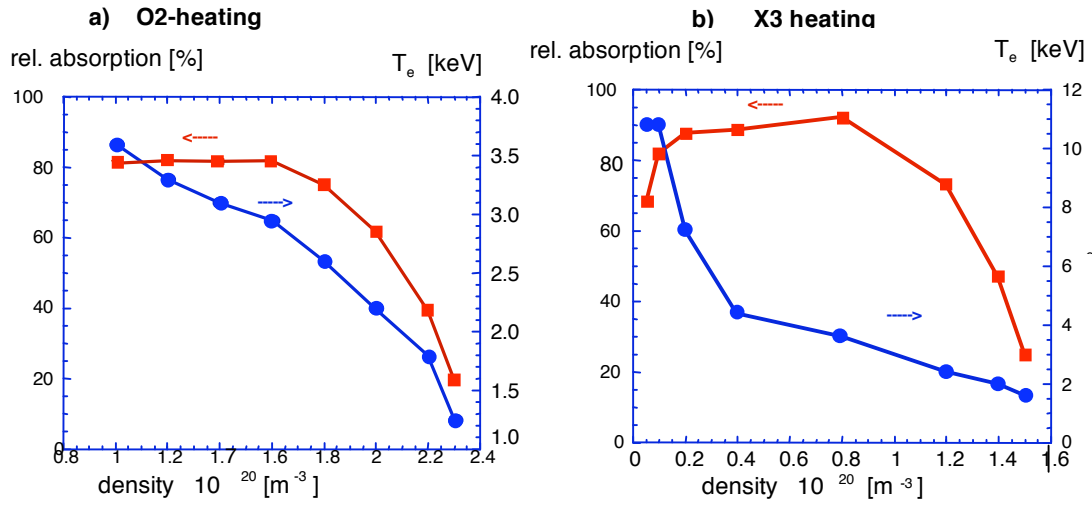
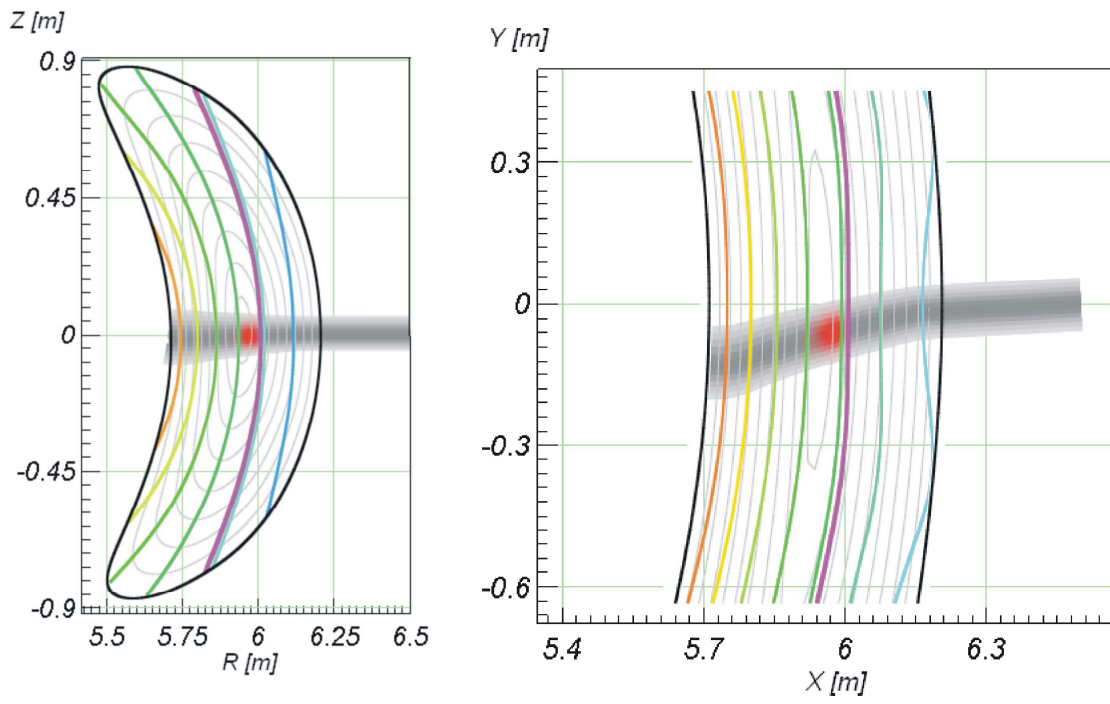


Figure 5



**Figure 6**



**Figure 7**

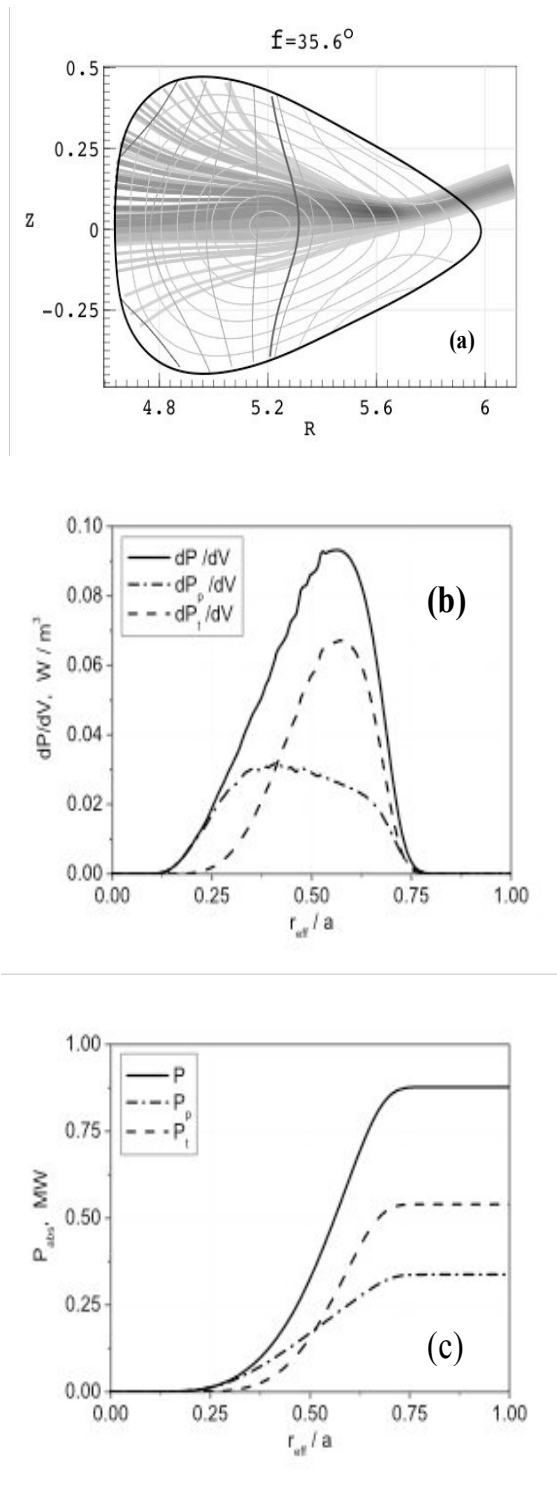
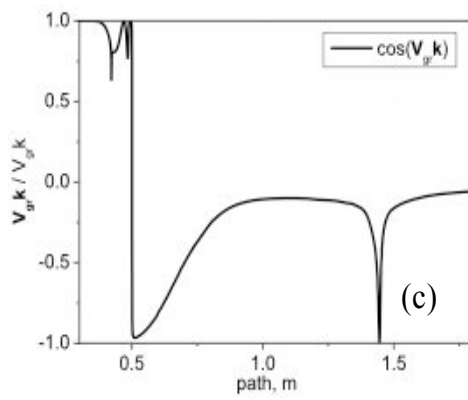
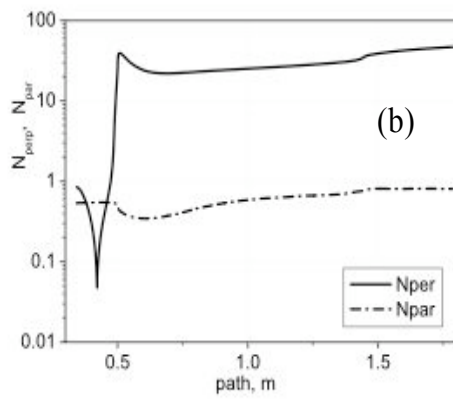
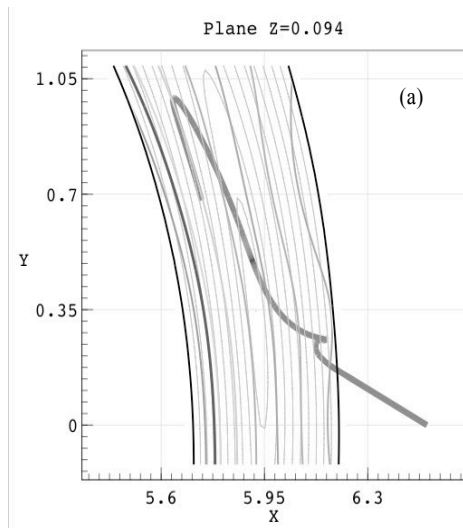


Figure 8



**Figure 9**

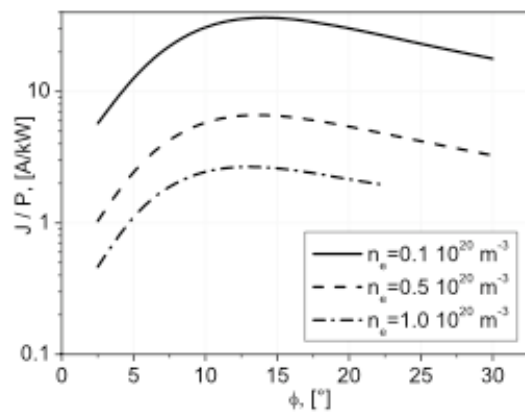
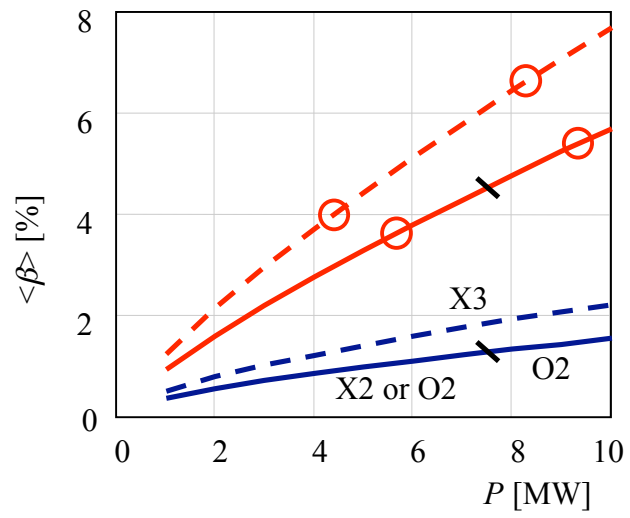
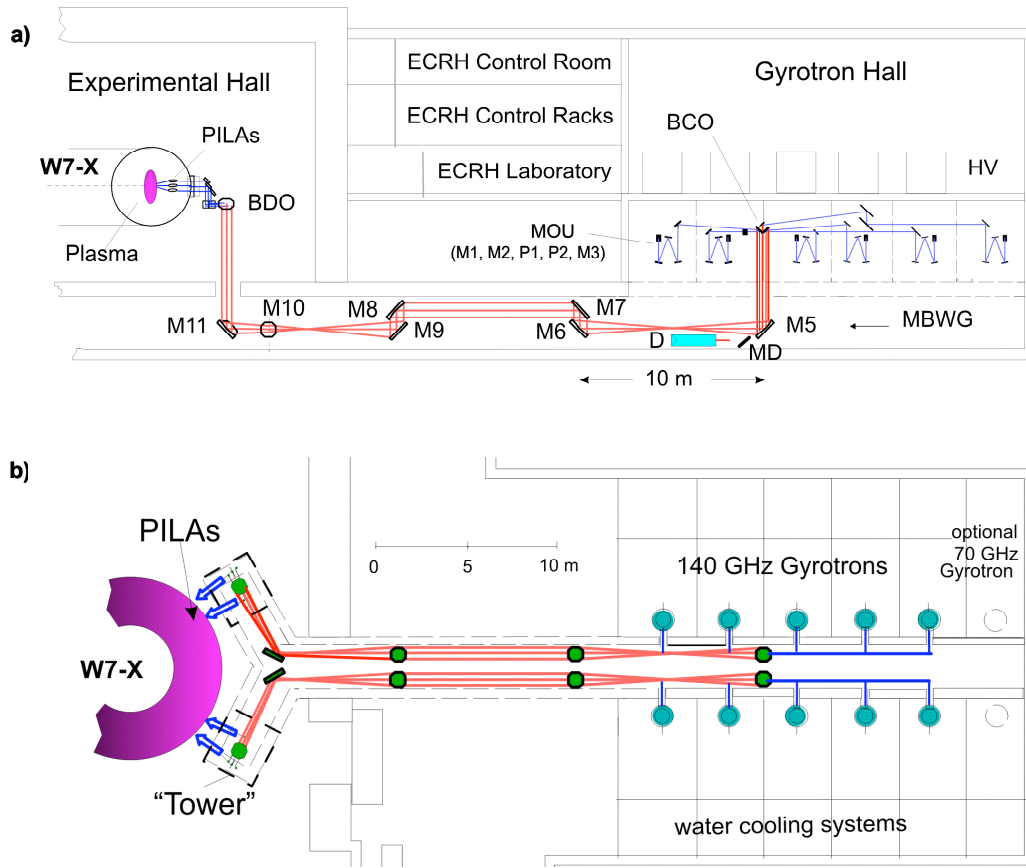


Figure 10



**Figure 11**



**Figure 12**

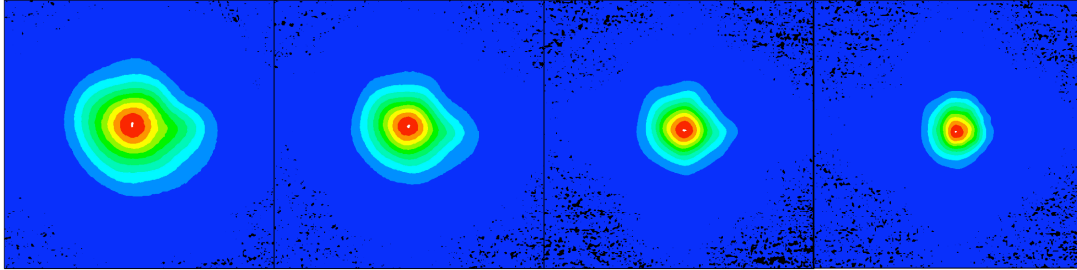
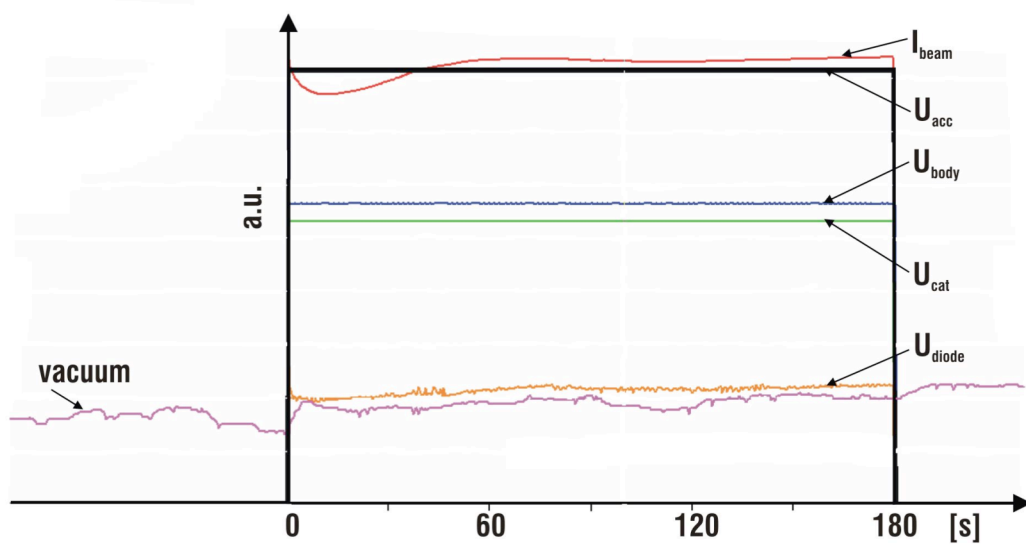


Figure 13



**Figure 14**



Figure 15

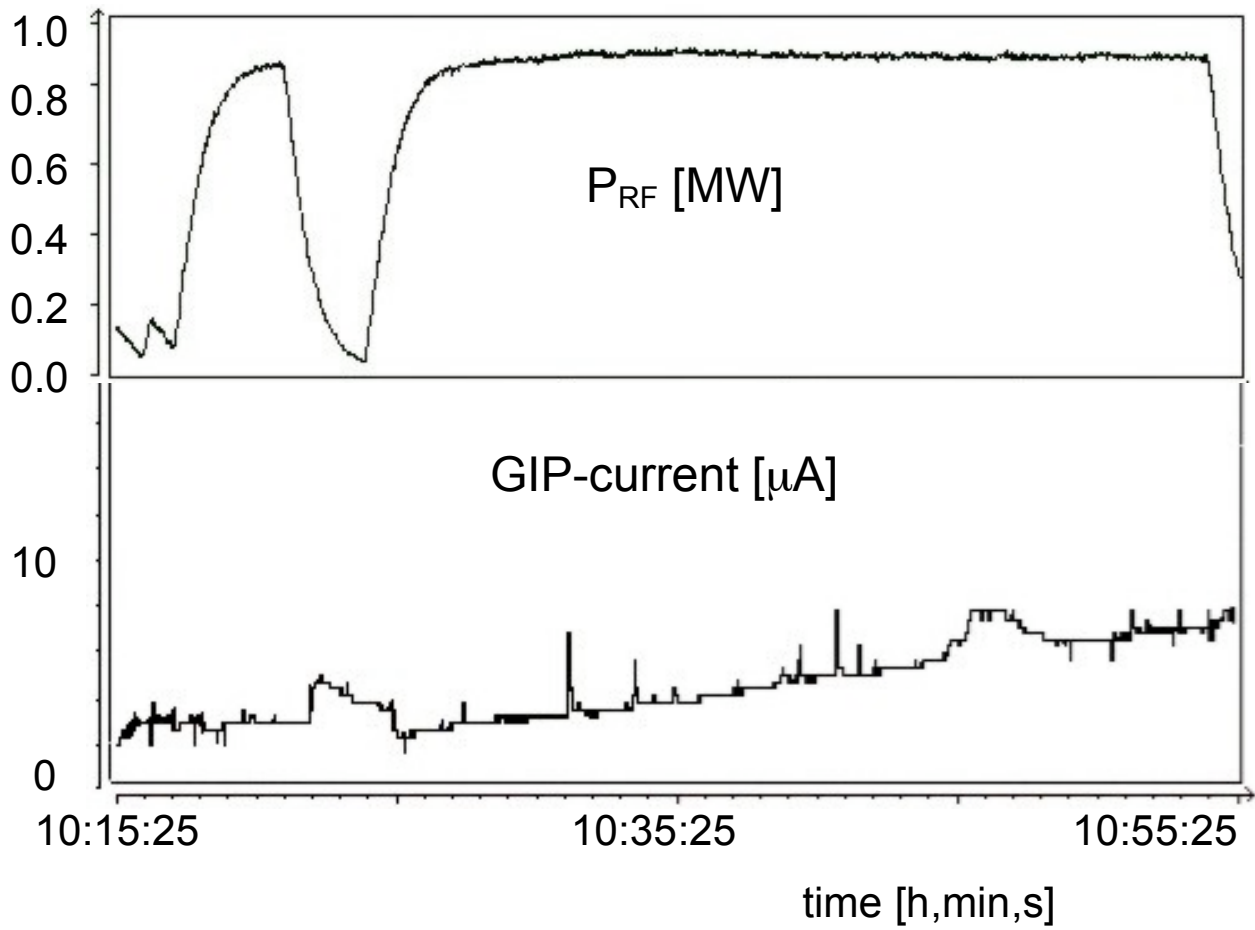
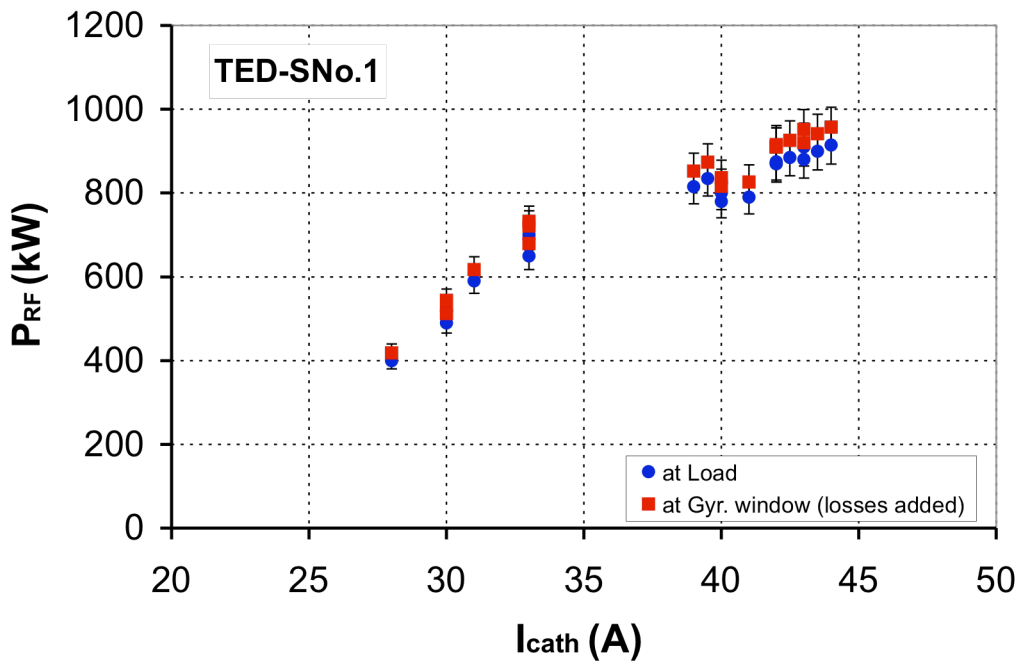
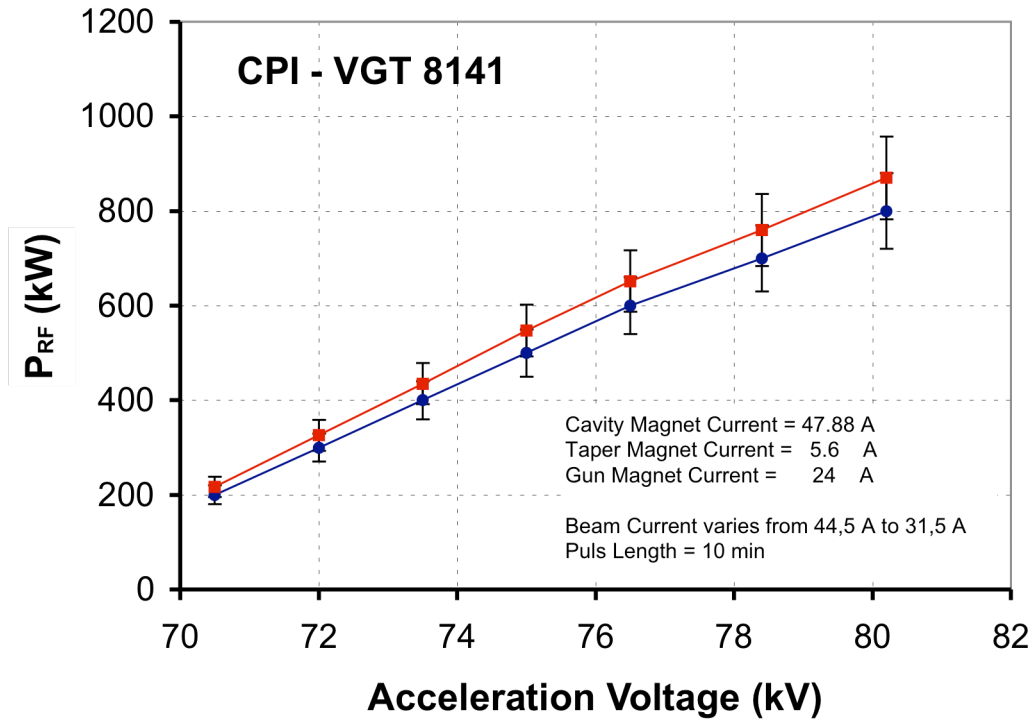
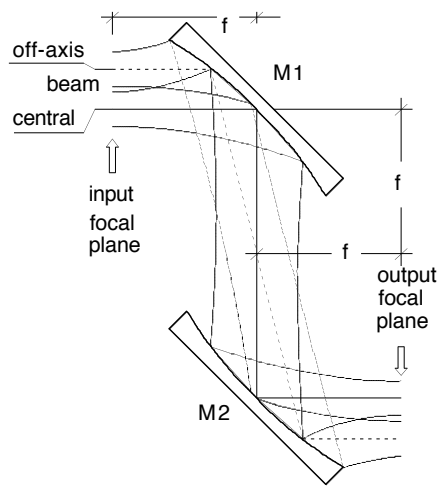


Figure 16



**Figure 17**



**Figure 18**

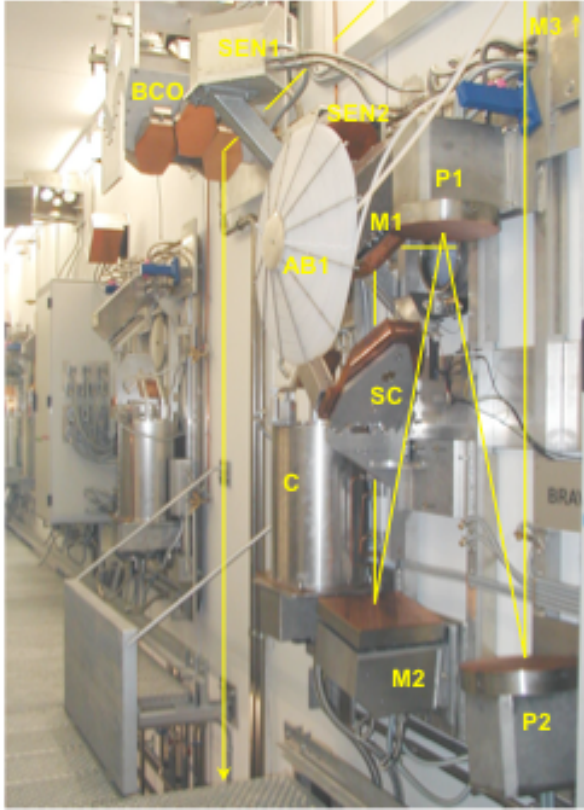


**Figure 19**



Figure 20

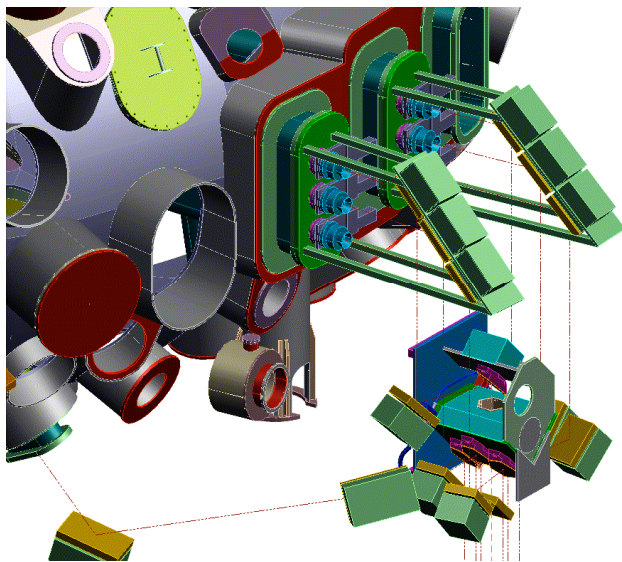
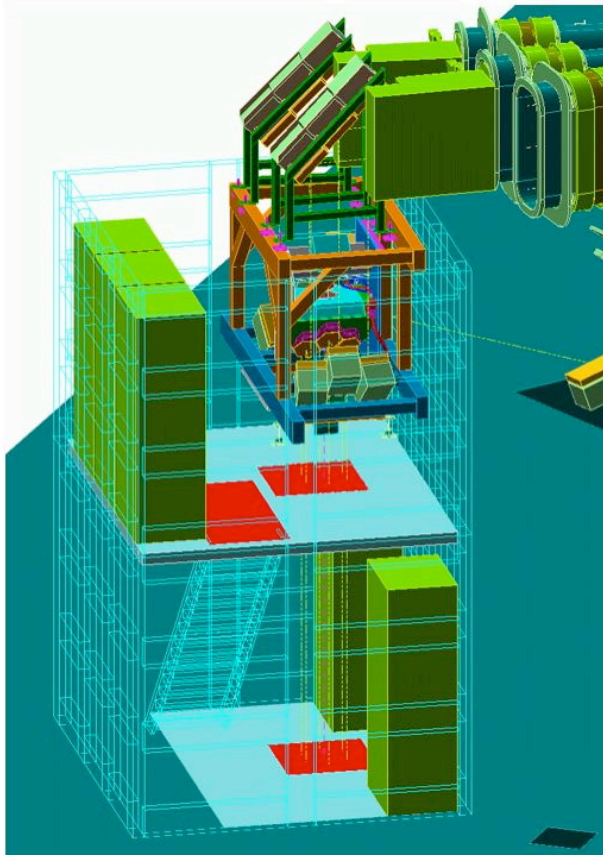


**Figure 21**



Figure 22

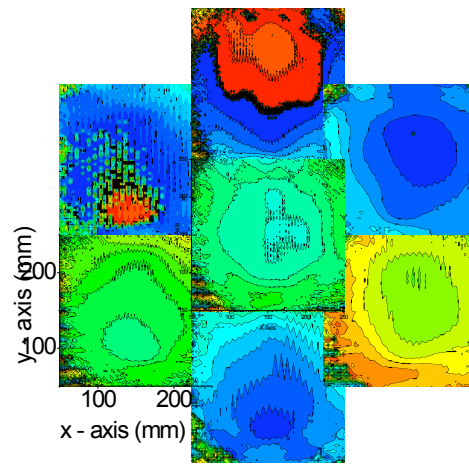
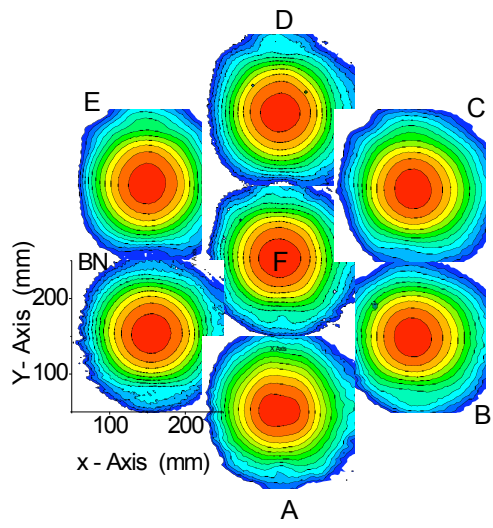
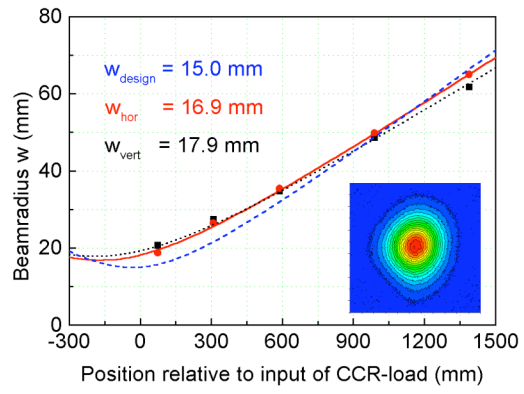


Figure 23



**Figure 24**

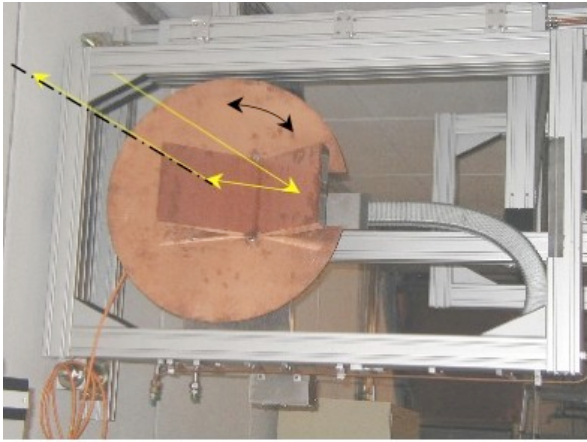


Figure 25

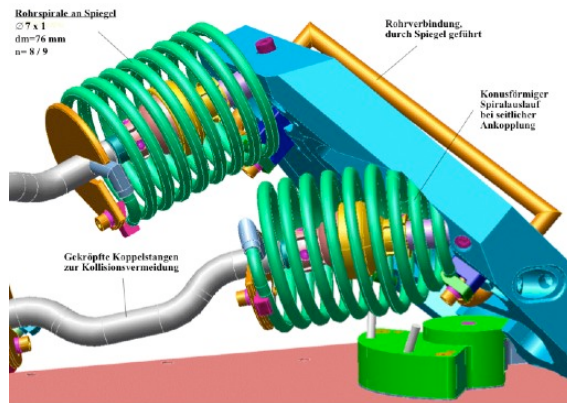
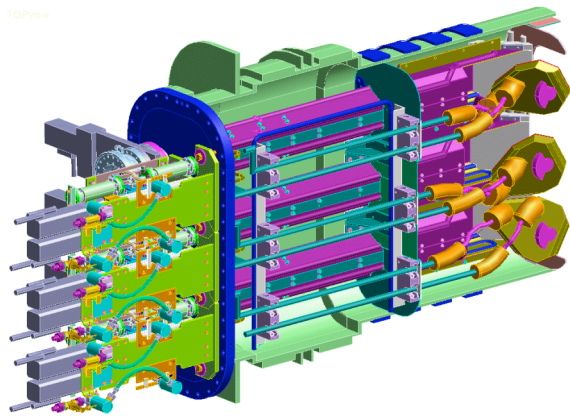
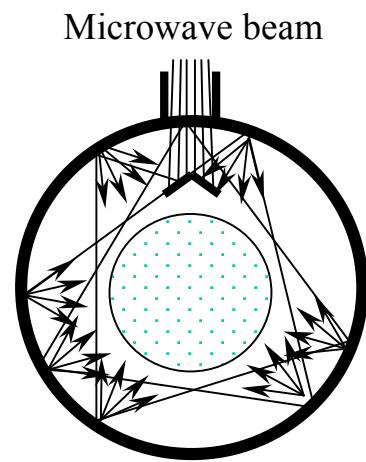
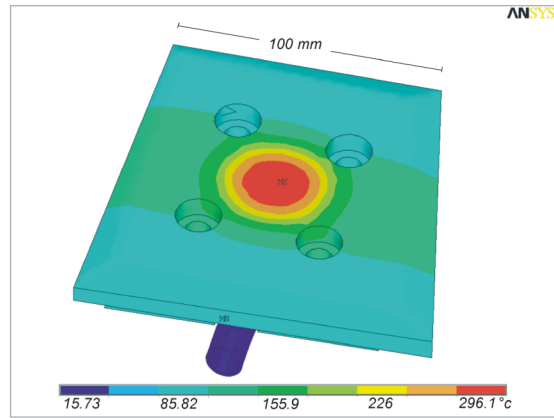
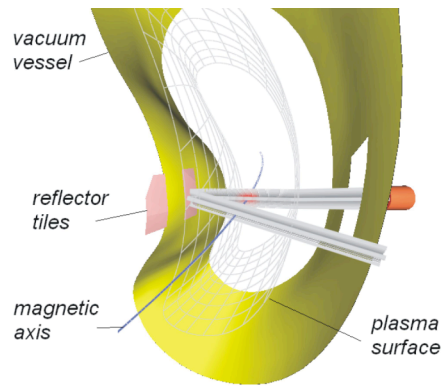


Figure 26



**Figure 27**



**Tables:**

	<b>W7-X</b>	<b>ITER</b>
Power (MW)	10	24
Power per gyrotron (MW)	1	1 (2)
Frequency (GHz)	140	170
Operation Mode (standard)	2nd Harm. (2.5 T) CW (1800 s)	1st Harm. (5.6 T) CW (1000 s)
Transmission	optical	waveguide
Launcher	Front steering	Front steering/ Remote steering
Physics demands	Bulk Heating and Current Drive q-profile shaping	Bulk Heating and Current drive q-profile shaping MHD-control
	Net-current suppression	Net-current enhancement

**Table I.** ECRH for W7-X and ITER, main parameters

	TED	CPI
RF output power (MW)	1	
Frequency (GHz)	140.2	
Operation	CW	
Power-Modulation (kHz)	< 10	
Accelerating voltage (kV)	81	82
Collector depression voltage (kV)	27	< 30
Beam current (A)	40	< 45
Cavity mode	TE <sub>28,8</sub>	TE <sub>28,7</sub>
Efficiency (%)	45	> 40
Cavity radius (mm)	20.48	19.26
Self consistent quality factor	1100	1130
Cavity magnetic field (T)	5.56	5.43
Launcher taper (mrad)	4	
Launcher efficiency (%)	98	

**Table II:** Design parameters for the TED- and CPI-Gyrotron

<b>Loss channel</b>	<b>(Number of) elements</b>	<b>Loss</b>
Absorption on mirrors	14 plane + 2 grooved Cu surfaces	2,5 %
Diffraction and beam truncation	16 reflectors	2 %
Misalignment	Transmission line	2 %
Atmospheric absorption	60 m dried air	0,8 %
Beam truncation, launcher	1 Window + 2 int. mirrors	3 %
<b>TOTAL LOSS</b>		<b>10 %</b>

**Table III:** Contributions to the transmission loss for the ECRH system on W7-X.